This is to certify that the

thesis entitled

THE EFFECT OF MICROSTRUCTURE AND TEXTURE ON THE MECHANICAL PROPERTIES OF DOUBLE-REDUCED TINPLATE STEEL

presented by

Michael David Wood

has been accepted towards fulfillment
of the requirements for

Master degree in Materials Science

Major professor

Date 6/21/94

THE EFFECT OF MICROSTRUCTURE AND TEXTURE ON THE MECHANICAL PROPERTIES OF DOUBLE-REDUCED TINPLATE STEEL

By

Michael David Wood

A THESIS

Submitted to
Michigan State University
in partial fulfillment of the requirements
for the degree of

MASTER OF SCIENCE

Department of Materials Science and Mechanics

1994

ABSTRACT

THE EFFECT OF MICROSTRUCTURE AND TEXTURE ON THE MECHANICAL PROPERTIES OF DOUBLE-REDUCED TINPLATE STEEL

By

Michael David Wood

The influence of microstructure and crystallographic texture of double-reduced tinplate steel was investigated in order to determine their effect on the mechanical properties. Double-reduced tinplate steel undergoes hot-rolling, cold-rolling, continuous annealing and further cold-rolling during its production, with the parameters of each step having an influence on the final microstructure and texture. Tinplate of two different thicknesses were examined, with both materials exhibiting a fully recrystallized ferritic microstructure. The dominant texture component present in the tinplate steel was the {111}<uvw> fiber texture, with a weak {100}<011> bcc rolling texture due to the additional cold-rolling operation. The microstructure and texture present lead to anisotropic properties in the material. Test specimens oriented at 0, 15, 30, 45, 60, 75 and 90° with respect to the rolling direction were tested, and exhibited a trend of increasing strength and decreasing elongation as the orientation varied from 0° to 90°. The trend in material properties is explained by the grain shape effects and slip system geometry due to the crystallographic texture.

ACKNOWLEDGMENTS

I would like to express my thanks to the faculty and students of the Department of Materials Science and Mechanics for all of their help and support during the course of this project. The guidance and friendship of my advisor, Dr. James P. Lucas, was greatly appreciated. I would also like to thank Dr. Tom Bieler, and his students Zhe Jin and Ramaswamy Saminathan, for their help and informative discussions concerning the subject of texture analysis. I would like to acknowledge the financial support and materials provided by The United States Can Company under grant 61-8502. Finally, I would like to thank my father and my sister for their constant support, without whom this would not have been possible.

TABLE OF CONTENTS

LIST OF TABLES

LIST OF FIGURES

INTRODUCTION

Low-carbon sheet steel is an extremely significant material used extensively in the consumer goods industries. No other material has been able to combine the capabilities of giving adequate strength and rigidity, being readily formed at high production rates into intricately shaped parts, providing an attractive surface after forming, and being easily joined to other parts through a variety of methods - all at a very low cost [1]. Low-carbon sheet steel is available in cut sheets, strips or coils and is either coated or uncoated. Uncoated sheet steel is very susceptible to oxidation, while steel coated with materials such as Zn, Al, Pb-Sn, Sn, Cr or various organic coatings exhibit considerable resistance to corrosion.

Even though sheet steel is such an important material, it has received a relatively small amount of attention by materials scientists outside of the steel industry. The reason that sheet steel has received such little attention is not due to the fact that its metallurgy is straight-forward or uninteresting, but rather because its metallurgical characteristics are developed at the steel mill, and the user need not be concerned with changing the composition or structure in order to realize its benefits. Sheet steel is actually a very complex material, and its properties are strongly affected by the composition and the processing parameters associated with its manufacture. It is the purpose of this study to characterize physical attributes such as microstructure and preferred orientation, and to determine their influence on the observed mechanical properties associated with commercially available low-carbon double-reduced tinplate steel.

Sheet Steel Production

Low-carbon sheet steel generally refers to material which has a thickness less than 0.230 inches containing less than 0.15% carbon. Figure 1 is a flow chart detailing the sequence of steps required in the production of sheet steel.

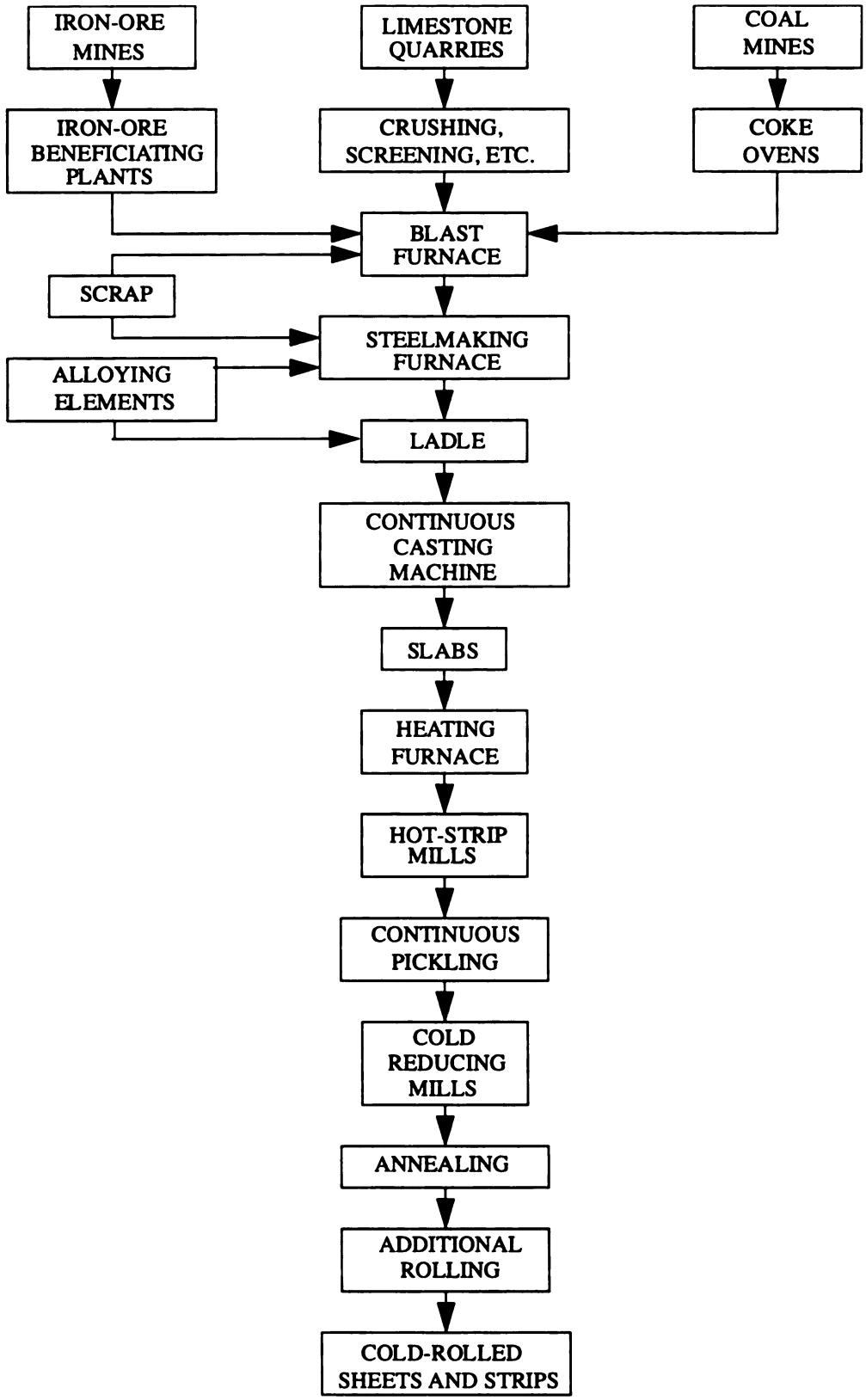

Figure 1: Processing of Steel Sheet

Iron-bearing materials, such as iron oxides, carbonates, sulphides and silicates, are the most important raw materials used in the production of steel. These iron ores are mined at various locations throughout the world, and are processed at beneficiating plants in order to improve their chemical and physical characteristics so that they are a more desirable feed product for the blast furnace. Methods used in the beneficiating process include crushing, screening, blending, concentrating and agglomerating. The crushing, screening and blending operations are performed in order to produce a more uniform product in terms of size. The concentrating and agglomerating steps involve washing and separating impurities from the ore, and are performed in order to improve the quality of the raw material. The result is a fairly uniform product in terms of size and quality which can be fed into the blast furnace for the production of pig iron.

While the iron ore beneficiating process improves the quality of the material being fed into the blast furnace, a considerable amount of impurities still exist in the ore. The production of crude iron involves two processes: the reduction of iron from its compounds, and its separation from the mechanical mixture. Many impurities existing in iron ores are refractory in nature, and are therefore difficult to melt. Flux materials are added to the blast furnace in order to make these impurities more easily fusible. Once fused, the impurities are either dissolved or chemically combined with the iron, and the secondary function of the flux material is to provide a substance with which the impurities can combine in preference to the iron. The chief flux material used is limestone, which is composed of calcium carbonate ($CaCO_3$), and dolomite, which is mostly calcium-magnesium carbonate ($(Ca,Mg)CO_3$). The limestone is typically crushed and screened in order to produce a uniform product which can be fed into the blast furnace.

Molten iron, or pig iron, is produced in the blast furnace by the reduction of iron oxides using the carbon of coke as the reducing agent. Coke is the residue resulting from the destructive distillation of selected coking coals at temperatures in the range of 900 °C to 1095 °C (1650 °F to 2000 °F). As the iron is reduced by the coke, it absorbs between

3.0 and 4.5 per cent carbon [2]. Since low-carbon sheet steel typically contains less than 0.15% carbon, the excess carbon is removed by controlled oxidation of mixtures of pig iron, melted iron and steel scrap in the steelmaking furnace. Various alloying elements, added to achieve desired properties in the final product, are added either during or after the carbon removal process. Most of the low-carbon sheet steel is produced by the basic oxygen and open-hearth steelmaking processes. The basic oxygen process refines the metal charge through the use of high purity oxygen. The oxygen combines with unwanted elements to form oxides which leave the molten bath either as gases or by entering the slag. The open hearth process is as the name implies, an open hearth, with great flexibility in terms of the fuel used for heating, and the relative amounts of scrap material which may be added to the charge.

After the molten metal has attained the desired chemical composition, it is tapped from the steelmaking furnace into a ladle. Additional alloying elements may be added at this point in order to yield the desired composition. From the ladle the molten metal is either poured into ingot molds and solidified, or transferred to a tundish for use with a continuous casting machine. Today, the most prevalent method for the production of slabs for the manufacture of sheet steel is continuous casting, depicted in Figure 2.

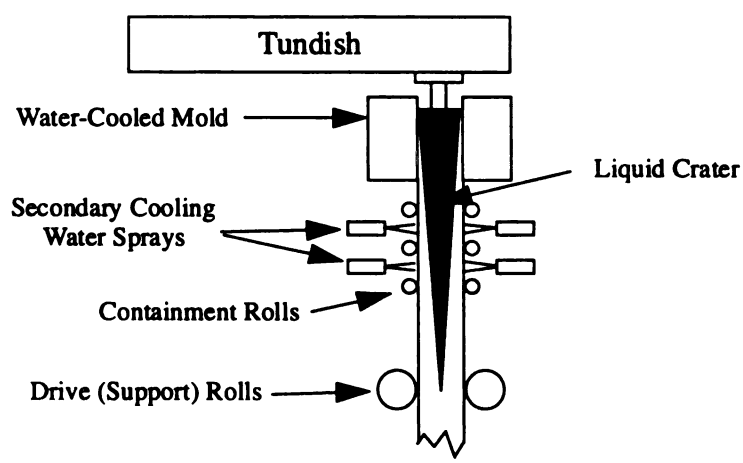

Figure 2: Continuous Casting Schematic [3]

The continuous caster consists of: a molten metal reservoir and distribution system, a water-cooled mold, a secondary cooling zone in conjunction with a containment section, a set of drive rolls in conjunction with bending and straightening rolls, a slab cutter, and a runout table to cooling beds or directly to the hot-strip mills [3]. To initiate the casting process, a dummy bar is inserted so that it closes off the bottom of the mold. The liquid metal is released out of the tundish at a controlled rate, and when the amount of metal reaches a predetermined level, the removal of the dummy bar is initiated. To prevent the solidified metal from sticking to the mold walls, the mold is oscillated vertically, and mold lubricants such as oils or fluxes are introduced. Before the dummy bar reaches the bending rolls, it is mechanically removed from the cast slab, and the casting process continues through the withdrawal system to the cutting equipment. The continuous casting process is favored over the ingot casting method for several reasons. The number of operations required to produce semi-finished shapes is reduced in the continuous casting operation, eliminating the need for stripping the ingots from molds, soaking the ingot until it reaches rolling temperature, and rolling the ingot to produce the semi-finished shape. Continuous casting also increases the yield from liquid steel to semi-finished shapes, eliminating crop losses from the top and bottom of the ingot, and scaling losses associated with heating the ingot in soaking pits [4]. The quality of continuously cast steel is also improved, leading to reduced variability in chemical composition and solidification characteristics, as well as improved surface quality and overall steel cleanliness.

The slabs produced by the continuous casting process are heated to 2300-2400 °F prior to the hot rolling process. The initial heavy reduction of the slabs occurs in the roughing mills, in which several four-high mills are used in tandem in order to achieve the large reductions. A four-high mill consists of large back-up rolls used to reinforce the smaller working rolls, as depicted in Figure 3. The smaller working rolls have less surface area in contact with the slab, and therefore impart greater pressure on the workpiece.

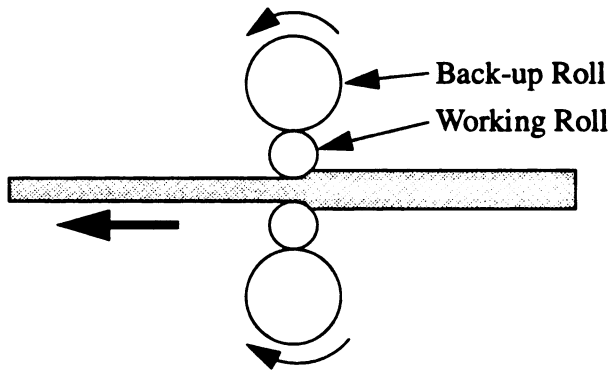

Figure 3: Four-high Roughing Mill [5]

The smaller rolls also resist the tendency of long working rolls to deflect, permitting the production of a uniform gage sheet. The slabs receive their final hot reduction in the finishing stands. The finishing stands also consist of several rolling mills operating in tandem, with the number of mills necessary being dictated by the final thickness desired after hot rolling. The mills used for finishing are typically cluster mills, in which several large back-up rolls are used to reinforce the smaller working rolls. The continuous strip emerging from the finishing stands is rapidly cooled through the use of water jets, and then coiled.

The hot rolling process leads to the formation of layers of iron oxide on the sheet surface, which must be removed prior to the cold reduction process by pickling the sheet in a hot solution of sulphuric acid. The oxide layer, if present on the surface of sheet used for drawing operations, will shorten die life, cause irregular drawing conditions and destroy the surface smoothness of the finished product. Sheet or strip materials which are to be coated must also have the oxide layer removed, in order to permit proper adherence of the coating material. The outermost layers of scale consist of Fe_2O_3 and Fe_3O_4, which are only slightly soluble in the acid solution [6]. The layer adjacent to the steel surface is known as wüstite, a decomposed ferrous phase consisting of a solid solution of iron and

oxygen. In order for the acid solution to attack the underlying decomposed ferrous phase, the coiled sheet travels through a series of rollers which stretch and bend the material, causing the outermost layers of oxide to crack. The cracked layers of oxide provide a passageway for the acid solution to penetrate to the decomposed ferrous phase. The continuous sheet then travels through a series of pickling tanks, where the acid attacks and dissolves the remaining oxide. After the pickling tanks, the sheet travels through cold water rinse tanks to remove the acid carry-over, and then a hot water rinse tank and hot air dryer. Prior to exiting the continuous pickling line, the sheet receives a thin oil coating, which serves to protect the material as well as reduce friction in the subsequent cold reduction mills.

Cold rolling is the process of passing unheated metal through a series of rolls for the purpose of reducing its thickness; producing a smooth, dense surface; and, with or without subsequent heat treatment, developing controlled mechanical properties. Since hot-strip mills cannot reduce the thickness beyond about 0.049 inches, the principle purpose of the cold reduction process is to reduce the thickness. Cold rolling yields a 25-90+% reduction in thickness from the hot rolled starting material. The cold reduction stand consists of several mills in tandem, each contributing to thickness reduction and driving the material being rolled. The speed of the successive rolls is such that the sheet is maintained under tension. Much greater pressures and driving forces are necessary to impart a given reduction as compared to hot rolling, and while the rolled sheet is unheated, considerable heat is generated during the rolling process. The heat generated is dissipated through the use of jets of oil directed at the roll bodies and the steel sheet. Upon exiting the cold reduction stand, the oil is removed from the sheet through the use of alkaline cleaners prior to being annealed.

Steel sheet is heat treated after the cold reduction process in order to effect changes in mechanical properties which render the material suitable for its intended purpose. While a small amount of steel sheet is used in the as-cold-rolled condition in order to take

advantage of the high strengths developed during rolling, most sheet materials receive some form of heat treatment to restore the ductility lost during cold reduction. The heat treatment typically consists of either batch annealing or continuous annealing. In the batch annealing process, coils or stacks of sheared sheets are placed in a controlled atmosphere "box" where the material is slowly ramped up to the annealing temperature, held at temperature, and slowly cooled to room temperature. This process is very time consuming, hence the development of the continuous annealing process. In continuous annealing, a single strand of sheet travels at high speed through a controlled atmosphere heating zone. The material is held at temperature for a very short period of time, and travels through a cooling zone so that it emerges into the air at a temperature low enough to avoid oxidation. The resulting product is typically harder than material subjected to batch annealing due to a finer resultant grain size and a larger amount of carbon and nitrogen retained in ferrite solid solution. In addition to the recrystallization zone, continuous annealing also includes an overaging zone, where the sheet is again heated to a lower temperature allowing for more complete precipitation of carbon from ferrite solid solution, increasing the ductility and reducing the tendency for strain aging in the steel sheet.

Sheet steel subjected to the above processing conditions exhibit the phenomenon known as the lower yield point, or yield point elongation. Upon deformation, the material forms stretcher-strain markings, or Lüder lines. These markings produce an undesirable surface appearance, therefore, the material is subjected to additional rolling to suppress the yield point elongation. An additional reduction up to 3% is termed temper rolling, and is also useful to impart the necessary surface finish, flatness, and to increase the strength to a specified minimum level. Some materials, such as double-reduced tinplate, undergo an additional cold reduction of as much as 20-30% in order to achieve the desired material properties.

Effect of Processing Conditions on the Structure and Properties of Sheet Steel

During the production of sheet steel, many factors affect the characteristics of the final product. While factors such as carbon content and chemical composition play an important role in the properties of sheet steel, the effects of the hot working, cold working and annealing operations on the structure and properties of the final product is vital in the understanding and characterization of low-carbon sheet steels.

Hot Working

Hot working is a term used to describe a deformation process which occurs above the recrystallization temperature of a material. As the material is deformed, dislocations are annihilated as well as generated, and deformed structures are recovered and recrystallized in-situ, yielding a retention of ductility in the deformed material. As a result of the maintained ductility, large deformations can be realized without the effects of strain hardening. When a cast slab of steel is hot rolled to a large reduction in thickness, the macroscopic and microscopic development of the structure, including the development of a preferred orientation due to the rolling process, must be understood and controlled, since the structure and, hence, the properties of the cold worked and annealed final product are dependent on the structure of the hot rolled strip.

Due to the high speed nature of the hot rolling process, equilibrium conditions do not exist [6]. The upper and lower temperatures for the transformation of austenite are reduced, the amount being dependent upon the cooling rate of the steel during rolling. Even though equilibrium conditions do not exist, the iron-carbon phase diagram is useful in explaining the microstructural changes occuring during the hot rolling process (Figure 4). The steel slab is heated to a temperature of 2300-2400 °F prior to receiving the initial heavy thickness reduction known as roughing . The roughing operation occurs in the

temperature range of 2300-1900 °F. In addition to the large thickness reductions which occur, the roughing operation also serves the purpose of refining the coarse grains which may have formed during the soaking operation.

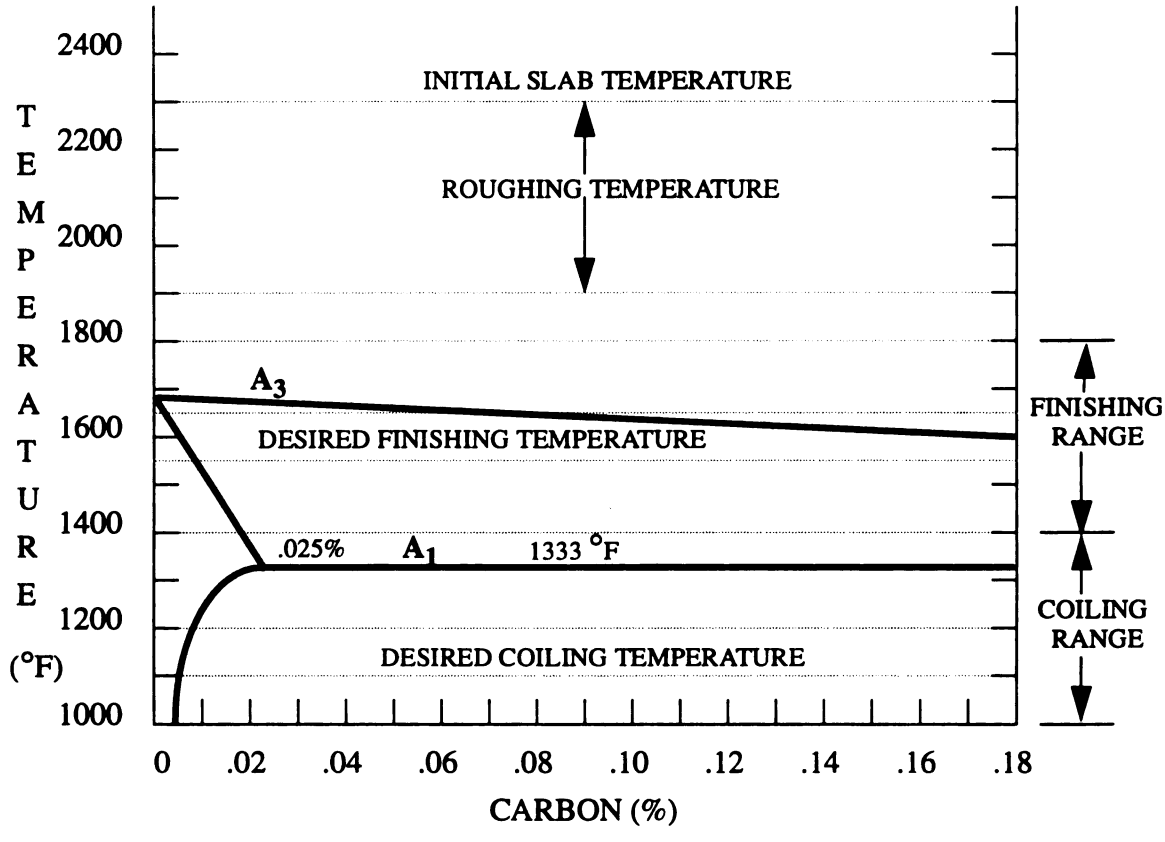

Figure 4: Portion of the Iron-Carbon Phase Diagram [6]

The slabs receive their final hot reduction in the finishing mills, with the temperature of the strip emerging from the last finishing stand known as the finishing temperature. The finishing temperature can vary between 1400-1800 °F, however, it is desirable for the finishing temperature to be above the transformation temperature of austenite to ferrite. If the strip exits the final finishing stand at a temperature above A_3 and is subsequently cooled rapidly, the resulting room temperature microstructure will consist of uniform equiaxed grains. During the hot rolling finishing process, the austenite grains are deformed and broken up. Between successive reductions, the grains recrystallize and

become finer and more equiaxed, the size of the grains being dependent upon the temperature of the steel and the time between reductions. The finer grain size is retained upon cooling to room temperature. If a portion of the hot rolling process occurs at a temperature below A_3, a mixed structure of ferrite and austenite is present, and two different types of abnormal microstructures may result, depending on the temperature at which the subsequent coiling operation takes place [6]. A coarse grain structure will result if the coiling temperature is high - about 1300 °F, due to the small amount of work hardening that would occur during rolling in the ferrite-austenite range. Even though the strip emerges from the finishing stand above the recrystallization temperature, recrystallization would not take place since slightly work-hardened steels require more time for recrystallization than do severely work-hardened steels. The result would be a coarse grain structure upon cooling to room temperature. If the strip is finish-rolled in the ferrite-austenite range and is subsequently coiled below the recrystallization temperature, the resulting microstructure upon cooling to room temperature will consist of deformed grains resulting from the hot-rolling process. After the final finishing stand, the emerging strip is cooled rapidly on a runout table using high pressure water sprays, and is coiled in the temperature range of 1000-1400 °F. At temperatures approaching 1300 °F, massive cementite particles may form during the coiling process, as shown by Rickett and Kristufek [7], leading to an adverse effect on the resulting mechanical properties and performance of the cold reduced annealed product. At lower coiling temperatures, the cementite particles formed are smaller and tend to form an aggregate with the present ferrite. As the coil cools below A_1, the solubility of carbon in ferrite is reduced, leading to the precipitation of carbides. The coiling temperature affects the size and distribution of the carbides. Higher coiling temperatures permit carbides to precipitate at a high temperature, allowing them time to grow in size while decreasing in number. A low coiling temperature shifts the precipitation to lower temperatures, so that the time and rate of diffusion are less and results in smaller, more uniformly dispersed carbide particles.

The finishing and coiling temperatures determine, to a large extent, not only the final microstructure of the hot-rolled strip, but also the resulting preferred orientation, or texture, of the hot-rolled product. The mechanism involved in the formation of the hot rolling textures is quite complex. As the material is deformed, factors such as the crystallographic nature of the deformation processes of slip and twinning, and the nature of the imposed stress (or strain) system associated with the rolling operation play an important role in the texture formed. However, since the material also undergoes an in-situ recovery and recrystallization, these factors will also affect the resulting hot-rolling texture. Proper hot-rolling and coiling conditions lead to a uniform, equiaxed microstructure with small, evenly distributed carbides resulting in consistent mechanical properties. When the sheet steel exits the finishing stand at a temperature above A_3, the resulting hot-rolling texture is a transformation texture due to the transformation of austenite to ferrite. Transformation textures have their origins in the orientation relationships betwen the parent and product phases. In the case of steel, the Kurdjumov-Sachs relationship [8]: $(111)_\gamma \parallel (110)_\alpha$: $[1\bar{1}0]_\gamma \parallel [1\bar{1}1]_\alpha$ relates the orientations of the γ (austenite) and α (ferrite) phases. As the material is deformed, the fcc austenite develops deformation texture components typical of fcc materials being deformed at room temperature, such as {112}<111>, {110}<112> and {123}<634>. Another texture component which may be present is the {001}<100> cube texture, which occurs if the austenite recrystallizes prior to the transformation to ferrite. The {112}<111> and {110}<112> texture components lead to {113}<110> and {332}<113> textures, respectively, after the transformation from austenite to ferrite, while the cube texture transforms to {001}<110>. The most predominant hot-rolling textures observed in sheet steel finish rolled above A_3 are the {113}<110> and {332}<113> texture components, with the {332}<113> component being the most beneficial in terms of achieving good deep drawability and improved strength and toughness [9]. While the optimum processing conditions dictate that the steel sheet exit the finishing stand above A_3, in

practice the finishing temperature is often in the ($\gamma + \alpha$) region. Rolling which occurs in the ($\gamma + \alpha$) region causes:

i) crystal rotation of the parent γ phase due to the rolling conditions

ii) $\gamma \rightarrow \alpha$ phase transformation, and

iii) crystal rotation and possible recrystallization of the product α phase.

The resultant texture of the steel is largely influenced by the relative contributions of the three above processes. The crystal rotation of the γ phase and $\gamma \rightarrow \alpha$ transformation are the same processes which occur when the steel is finish rolled above A_3, and the texture components developed are as previously described. When the finishing temperature lies in the upper ($\gamma + \alpha$) range, the amount of α phase formed before exiting the finishing stand is relatively small, and the contribution of the crystal rotation and recrystallization of the α phase to the resulting texture is insignificant. However, if the finishing temperature lies in the lower ($\gamma + \alpha$) range, most of the γ phase has transformed to α before exiting the finishing stand. The ferrite grains formed at higher temperatures, which have already inherited the γ rolling texture, are further deformed at lower temperatures. The additional deformation sharpens the texture of the α phase, while any remaining austenite grains are continuously deformed, resulting in an increase in the sharpness of the γ texture, which is eventually inherited by the transformed α phase. According to Bramfit and Marder [10], the texture developed in steels as a result of rolling below A_3 consists of two major components: i) a partial fiber texture having <110> axes parallel to the rolling direction with orientations lying in the range between {001}<110> and {111}<110>; and ii) the {111}<uvw> fiber texture. A considerable amount of {100}<011> may also be present due to the grain rotations occuring in the deformed α phase.

The resultant texture and microstructure of the hot-rolled strip plays an important role in the final texture and properties obtained after the cold-rolling and annealing operations. The texture present after the continuous annealing cycle depends on the parameters of the annealing process, and on the texture and microstructure of the cold-rolled material. In

turn, the cold-rolling texture and microstructure is dependent on the hot-rolling texture and microstructure. The transformation texture associated with finish rolling above A_3 is relatively weak in comparison to the texture formed when finishing occurs in the $(\gamma + \alpha)$ range. However, Vanderschueren, VanHoutte, et. al. [11] have shown that these transformation-type and deformation-type hot-rolling textures yield almost identical subsequent cold -rolling textures, with the exception of a higher intensity at the {001}<110> orientation associated with the deformation-type hot-rolling texture.

Cold Working

Cold-rolling is a generic term applied to passing unheated metal through rolls for the purpose of reducing its thickness; producing a smooth, dense surface; and achieving desired mechanical properties, either with or without subsequent heat treatment. Although the metal is unheated, a considerable amount of heat is generated due to the friction involved in the rolling process. The heat is dissipated through the use of oil lubrication jets directed at the rolls, and the resulting temperature falls far below the recrystallization temperature of the metal. Each pass in the cold reduction process must exceed the elastic limit of the material when considering the resultant of the compressive forces imposed by the rolls as well as the tension along the length of the strip between the reels and rolls [12]. The plastic deformation is primarily accomplished by the motion of dislocations and by shearing processes such as twinning. The structures and resulting properties which develop during plastic deformation depend on factors such as the crystal structure of the metal, the amount of deformation, the composition, the deformation mode, and the deformation rate. As a consequence of the symmetry involved in the cold-rolling operation, deformation textures are formed where certain crystallographic planes rotate and align parallel to the rolling plane, and certain directions align parallel to the rolling direction, which also has a significant effect on the resulting properties of the material.

The nature of the plastic deformation of a material during an operation such as cold-rolling is dependent upon the crystal structure of the material. Hot-rolled steel strip entering the cold reduction process primarily consists of ferrite, α-iron, which has a body-centered cubic crystal structure (bcc), as shown in Figure 5. The predominant process occuring during plastic deformation of metals is slip of adjacent planes of atoms

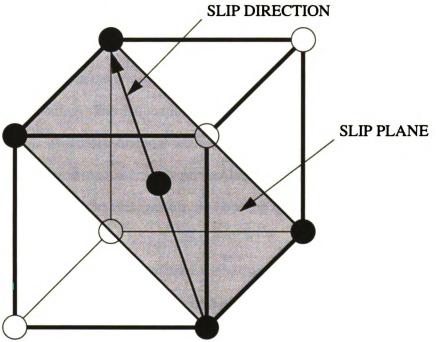

Figure 5: Body-Centered-Cubic Unit Cell

within the crystal. The crystallographic planes on which dislocations move and the unit displacement of dislocations (Burgers vector) are determined by the crystal structure. A typical <111>{110} bcc slip system is depicted in Figure 5. Slip has been reported by glide of dislocations with a Burgers vector of 1/2 <111> on {110}, {211} and {321} planes yielding 48 possible slip systems, however, it is generally considered that slip occurs on any plane containing a <111> slip direction, known as pencil glide.

Plastic deformation of polycrystalline materials begins with single slip in a few grains whose orientation yields a high Schmid factor. As deformation continues, single slip is initiated in more grains, which results in increasing misfits at the grain boundaries. The elastic strains created by the grain boundary misfit are accomodated in the material in the form of reaction stresses, which give rise to the activation of other slip systems. After a relatively small amount of plastic deformation, a state of polyslip exists in all of the grains. As a result of polyslip, dislocations begin to interact with one another, forming dislocation tangles. The interaction of dislocations, as well as the creation of additional dislocations in the material, raises the stress required to cause additional deformation, which is termed strain hardening. The dislocation tangles formed eventually delineate deformation cell walls [1]. Three-dimensional walls of dislocation tangles form a cell structure around uniformly sized areas of nearly perfect lattice. The dislocation walls are often parallel to a slip plane, with the average spacing between the walls decreasing as the strain increases.

As the amount of plastic deformation continues to increase, dislocation glide, cell formation and reduction in cell size can no longer describe the resulting microstructure. Deformation within individual grains becomes increasingly inhomogeneous because each grain must conform to the macroscopic shape changes which occur at large deformations. The microstructural features appearing at large deformations include deformation bands, transition bands, kink bands, microbands and shear bands [13]. Deformation bands are regions of different orientation within a single grain. Adjacent deformation bands are connected by transition bands, with continuous orientation changes through the thickness of the band. Kink bands are deformation bands separating regions of identical orientation. Microbands are long, straight bands of highly concentrated slip lying on the slip planes of individual grains. Microbands are typically 0.1 to 0.2 μm thick, traverse an entire grain, and correspond to the slip bands seen on the surface of a polished specimen. Shear bands are regions of very high shear strain. During the rolling process, strain bands form at ~

±35° to the rolling plane, parallel to the transverse direction. At high strains, strain bands traverse the entire thickness of the rolled sheet material.

The microstructural changes which occur as a result of the cold-rolling operation are accompanied by the formation of a deformation texture. Deformation textures have their origins in the crystallographic nature of the deformation processes occuring during deformation. At large strains, slip is usually the major factor, however twinning can also have a significant contribution because of the massive re-orientations involved. During rolling, the operation of shear on a slip system causes crystal lattice rotations as a result of the shape change and the geometrical constraints of the process. The restricted number of slip systems available produces rotations towards a limited number of end-points. Continuing deformation causes additional rotation until eventually stable orientations are reached where rotation is not a requirement for additional slip. The final deformation texture consists of the stable orientations (components) which result from all possible initial crystal orientations. The strength of the individual components depends on the proportion of original crystal orientations which rotate to that end point, which is affected by any previous texture existing in the material.

During cold-rolling of low carbon sheet steel, the texture of ferrite becomes progressively stronger and sharper with increasing deformation, however, the main components that develop are almost independent of the material and processing variables. The cold-rolling texture of steel is comprised of two major orientation spreads [14,15]. One component is the γ fiber, with {111} planes parallel to the sheet surface and a continuous spread of orientations from <110> to <211>, depicted as {111}<uvw> and typically referred to as the cube-on-corner texture. The other major spread is a partial fiber texture with <110> parallel to the rolling direction. encompassing the orientations {001}<110>, {112}<110> and {111}<110>. The {111}<$\bar{1}$10> and {001}<110> textures are depicted schematically in Figure 6.

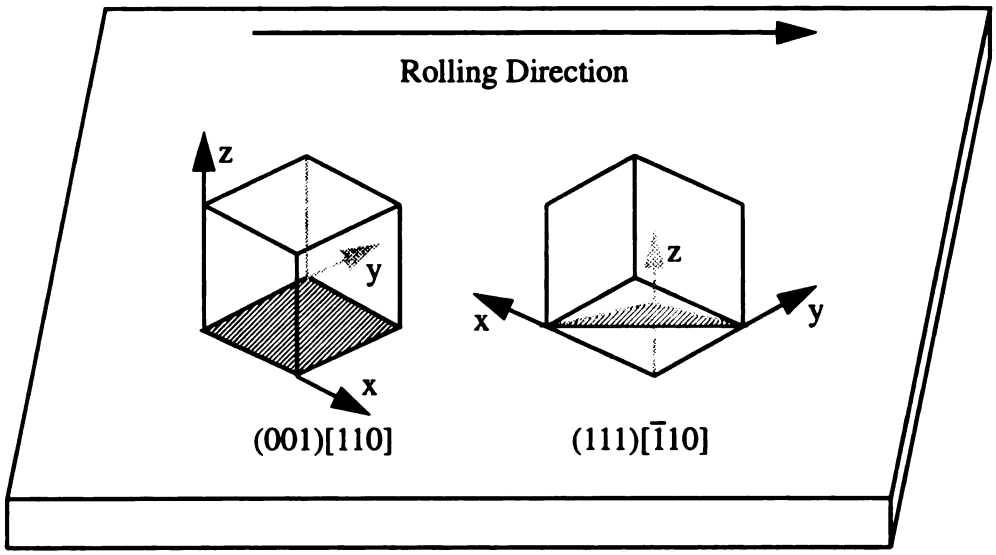

Figure 6: Typical bcc Deformation Textures [16]

Annealing

The cold reduced sheet steel is subjected to a continuous annealing stage, which serves the purpose of restoring ductility to the deformed material. The internal stored energy and dislocation structures present in the various deformed grains of the cold-rolled sheet represent the driving force for recovery and recrystallization on annealing. In the recovery stage, the steel reverts to a condition in which the mechanical and physical properties tend towards the undeformed state. During the initial stages of recovery, little change occurs to the microstructure and properties of the steel. As recovery continues, the dislocation density decreases while a dislocation network of subgrains is formed [1]. The subgrains which are formed have low-angle boundaries comprised of low-energy dislocation arrays, rather than the dislocation tangles associated with the deformed material. Once the dislocation rearrangement is complete, the cell size increases by either a process of

subgrain boundary migration [17] or coalescence [18]. The new subgrain boundaries are higher-angle, higher-energy boundaries, however, the total boundary area and dislocation density have decreased. The subgrains slowly increase in size until they have mobile high-angle boundaries, at which time they can act as the nuclei of recrystallized grains. Recrystallization begins when the high-angle boundary subgrains begin to grow at the expense of neighboring subgrains to form new grains that are relatively free of substructure. The resulting microstructure obtained after the continuous annealing cycle is fully recrystallized ferrite.

During the processes of recovery and recrystallization, the deformed material undergoes microstructural changes, and new grains are nucleated and grow at the expense of the deformed matrix. The changes which occur within the material also cause a change in the preferred orientation. Various theories have been proposed as to the mechanism by which the changes in texture occur. Some believe that the annealing texture is established by the formation of nuclei of specific orientations, the oriented nucleation theory, and these preferentially oriented nuclei grow without competition from nuclei of different orientations. The oriented growth theory states that nuclei of all orientations are formed, and that some nuclei grow faster than others, depending on their orientation relative to the recovered matrix. According to the literature, the theory which seems to best explain the phenomena of annealing texture formation involves elements of both oriented nucleation and oriented growth [19,20]. During the process of recovery, the individual crystallite orientations are modified very little, and the deformation texture is retained. In a study conducted by Dillamore, et al. [21], it was shown that the relative amounts of stored energy in the components of the rolling texture influence the formation of the recrystallization texture. The cell size and cell-boundary misorientation measured by transmission electron microscopy in iron cold-rolled to 70% reduction varied in a systematic way according to the deformed grain orientation. Fine cells with large misorientations occurred in the {111} family, while the cells became coarser and more

oriented closer to the {001}<110> component. The stored energy of deformation therefore increased in the order {001} < {112} < {111}. Nucleation by subgrain growth mechanisms within individual deformed grains is most rapid where the stored energy is greatest, and favors nucleation within {111} oriented grains. The recrystallized orientation is also {111}, however, it should be noted that the recrystallization texture formed is related to the original deformation texture, often by rotations about simple crystallographic directions, but not usually identical. At some point after the {111} grains have started to recrystallize, the remaining orientations recrystallize according to their relative amount of stored energy. The recrystallization ordinarily occurs at the as-rolled grain boundaries, and the grains grow by absorbing the remaining unrecrystallized orientations. Therefore, the intensity of the {111} component remains relatively constant in comparison to the deformation texture, or shows a slight increase, while the {100} components of the rolling texture decrease considerably. Dillamore and co-workers also showed that {111} oriented grains tend to form subgrains more readily than {100} deformed grains. After recrystallization the {100} grains are smaller than the {111} grains, and during the process of grain growth the {100} oriented grains are consumed by the larger {111} grains. As a result, the texture of the annealed sheet steel product retains the {111}<uvw> fiber texture which was present in the cold reduced material, and the {100}<011> component of the partial fiber with <011> parallel to the rolling direction is significantly reduced in intensity.

EXPERIMENTAL PROCEDURES

Materials:

The material used in this study was double-reduced tinplate steel, conforming to A.S.T.M. A-623, Type L, and was supplied by The United States Can Company. The chemical composition requirements, as stated in A.S.T.M. A-623, for Type L tinplate are listed in Table 1.

Table 1: Chemical composition of Double-Reduced Tinplate Steel, Type L

Element	Composition max. %
Carbon	0.13
Manganese	0.60
Phosphorous	0.015
Sulfur	0.05
Silicon	0.020
Copper	0.06
Nickel	0.04
Chromium	0.06
Molybdenum	0.05
Residuals	0.02

Double-reduced tinplate steel is produced from continuous cast steel slabs. The cast slabs, ranging in thickness from 4 to 10 inches, are hot-rolled at an elevated temperature to a single continuous length which is coiled. The coiled product is typically 0.070 to 0.100 inches in thickness. The hot-rolled product exits the last finishing stand at a temperature in the range of 1500 to 1600 °F, is cooled through the use of water jets, and enters the coiler at a temperature of 1100 to 1250 °F. The hot-rolled product is continuously pickled in an acidic solution to remove all of the scale and oxide from the surface and is subsequently oiled prior to cold reduction. The pickled product is cold-rolled 80 to 90 percent on five-stand or six-stand four-high tandem cold-reduction mills. The cold-reduced product is continuously annealed in a protective atmosphere at approximately 1200 °F in order to soften the material and increase its formability. The annealed strip is cold-rolled an additional 30 to 40 percent, yielding a product with high hardness, yield strength and tensile strength, yet still possessing sufficient formability for a wide range of applications. The final reduced product receives an electrolytic tin coating with a thickness in the range of 83 - 275 μm, which is melted to give a lustrous appearance. The two materials investigated in this study were 62 #/base box and 78#/base box[1] tinplate steel (0.0068 inch and 0.0086 inch thickness respectively). The difference in end product thickness is achieved at the hot-rolling stage, with thinner gage end products receiving larger hot-rolling reductions. The amount of cold reduction and additional reduction subsequent to the annealing process is typically held constant (i.e. 90% cold reduction and 30% additional reduction) in order minimize the variation in properties.

---

1. Tin mill products are ordered to thicknesses expressed in base weight units. The base weight is the weight, in pounds, of one base box (a unit of area equivalent to 112 sheets 14 by 20 in. or 31,360 in.^{2}) which is a measure of the approximate thickness.

Microstructural Analysis

The microstructure of the sheet stock materials was characterized by cold mounting specimens using a two-part room temperature curing epoxy resin system. Three specimens for each thickness material were mounted such that the sheet normal, on-edge in the rolling direction and on-edge perpendicular to the rolling direction microstructures could be observed, as shown in Figure 7.

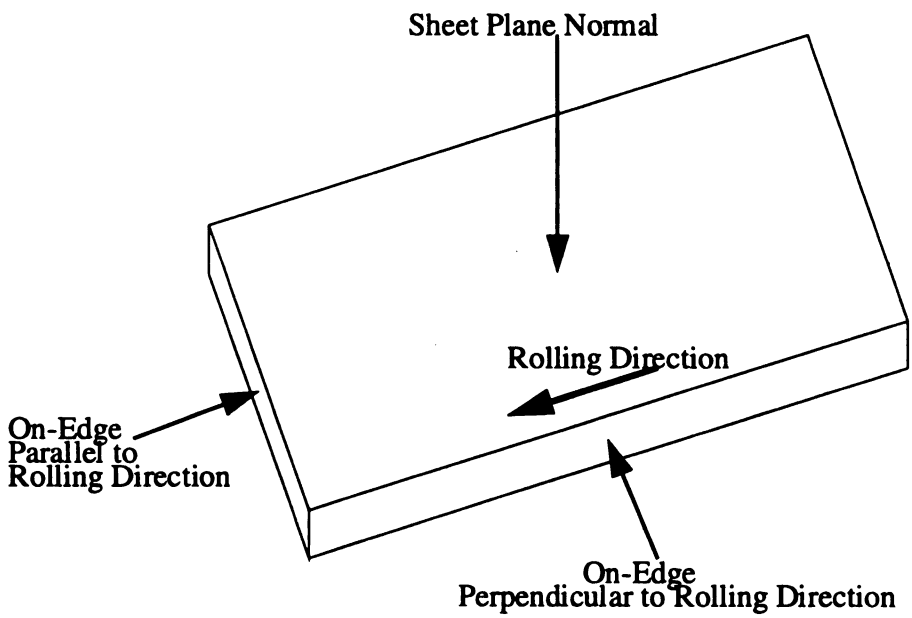

Figure 7: Location of Microstructural Characterization Samples

The mounted samples were mechanically ground using progressively finer stationary abrasive papers of 240 grit, 320 grit, 400 grit and 600 grit. The samples were thoroughly rinsed between grinding stages to remove residual abrasive. The ground specimens were then polished using Leco VP-150 polishing wheels in conjunction with 600 grit, 5 μm, 0.3 μm and 0.05 μm Al_2O_3 abrasive suspended in distilled water. Once again, the samples were thoroughly rinsed between polishing steps in order to avoid carry over of residual abrasive to subsequent polishing steps. The polished specimens were etched using a 3%

Nital solution (3% Nitric acid, remainder Methanol) for approximately 20 seconds to reveal the sheet steel microstructure. The microstructure of the polished and etched specimens was photographed using an Olympus PME3 optical microscope equipped with the PM-10AK automatic exposure photomicrographic system and Polaroid camera attachment.

The grain size in the width, height and length of the elongated grains was determined using the line intercept method:

$$GS = \frac{L}{n \times M}$$

where: GS = average grain size
L = length on intercept line
n = number of grains intercepted
M = microscope magnification

The number of grains intercepted was determined by drawing 5 lines of equal length in each respective direction, and computing the average number of grains traversed. The magnification used for the grain size calculation was determined through the use of a marker of fixed length located inside the microscope which appears on the photograph. The marker was manually measured using a scale with 0.01 inch increments to determine the actual magnification. The aspect ratio of the grains was determined by dividing the average grain width by the average grain height. The average grain volume was calculated using the average width, height and length of a grain in conjunction with the formula for the volume of an ellipsoid:

$$V = \frac{4}{3}\pi wlh$$

where: w = width
l = length
h = height

The average number of grains through the thickness of the materials was determined by dividing the material thickness by the average grain height.

The fracture morphology of 62# and 78# plate materials was characterized using a Hitachi S-2500C Scanning Electron Microscope (SEM). A tensile sample with the tensile axis parallel to the rolling direction was tested to failure, and the failed region of the sample was mounted on an SEM stage using carbon paint. Micrographs of the fracture surface were taken using the polaroid camera attachment of the SEM.

Mechanical Testing

The mechanical strength properties of the double-reduced tinplate steel were determined through the use of several different techniques. Standard tensile tests, high strain-rate tensile tests, r-value tensile tests and three-point bending flexure tests were performed on specimens of varying angle with respect to the rolling direction. Samples for the standard tensile tests were supplied by The United States Can Company. Test samples for the high strain-rate, r-value and flexure tests were produced from supplied sheet materials.

Standard tensile tests were performed on 62# plate and 78# plate specimens oriented at 0, 15, 30, 45, 60, 75 and 90° with respect to the rolling direction in accordance with the ASTM E8-83 testing procedure. Five specimens were tested at each orientation. The testing was performed on an Instron model 4302 bench-top universal testing machine using wedge-action grips and a 2 inch gage length extensometer. Instron series IX data reduction software was used for the calculation of the 0.2% offset yield stress, the peak stress, the Young's modulus and the percent plastic elongation at break. The strain hardening exponent was determined manually according to ASTM E646. Five equally spaced points were chosen on the stress-strain curve between a location where the curve began to exhibit non-linearity in the elastic region and the peak stress. The stress-strain

data pairs were converted to true stress and true strain, their logarithm taken, and the strain hardening exponent, n, determined through linear regression analysis. The angle of fracture with respect to the tensile axis was manually measured on each tensile specimen by tracing the outline of the fracture surface and the gage length region and measuring using a protractor.

High strain-rate testing was performed using an MTS series 810 servo-hydraulic testing machine in conjunction with a Nicolet model 4094B digital storage oscilloscope. Tensile specimens with 0.5 inch gauge lengths and 0.5 inch widths having orientations of 0, 15, 30, 45, 60, 75 and 90° with respect to the rolling direction were tested at a strain rate of 1×10^2 sec^{-1}. Test specimens were prepared by initially shearing rectangular strips from the steel sheet, then routering the gage length section using a Tensilkut test specimen preparation machine and associated specimen cutting fixture. The specimen dimensions were taken using calipers with 0.01 inch increments. Real-time displacement and load data was collected by attaching lead wires from the displacement and load transducers of the MTS to the appropriate channels of the oscilloscope. Load vs. displacement data points were taken manually from the storage oscilloscope and converted into stress vs. strain data points and plotted.

The value r refers to the plastic strain ratio, which is an estimate of the ratio of plastic strains in the plane of the sheet and perpendicular to the sheet. The plastic strain ratio is a very useful parameter used to determine the deep-drawing capabilities of materials. Press forming and deep drawing are very common methods used to produce parts from sheet materials, and require maximum plastic flow in the plane of the sheet while providing maximum resistance to flow in a direction perpendicular to the sheet. An estimate of the ratio of strains in the plane of the sheet and perpendicular to the sheet can be obtained in a simple tension test from a ratio of the true strains in the width and thickness directions according to:

$$r = \frac{\varepsilon_w}{\varepsilon_t} = \frac{\log \frac{w_o}{w_f}}{\log\left(\frac{w_f \cdot l_f}{w_o \cdot l_o}\right)}$$

where: ε_w = true width strain
ε_t = true thickness strain
w_o = original width
w_f = final width
l_o = original length
l_f = final length

The physical meaning of r is such that r = 1 indicates equal flow strengths in the plane and across the thickness of the sheet; r > 1 indicates the average strength in the plane of the sheet is lower than across the thickness; and r < 1 indicates higher strength in the plane of the sheet than across the thickness. For deep drawing applications, an r value greater than unity is desirable because the material will resist thinning during the drawing operation.

R value determination tests were performed on 0.5 inch gage length tensile specimens oriented at 0, 15, 30, 45, 60, 75 and 90° with respect to the rolling direction. The specimens for the r-value determination tests were produced in the same fashion as those used for the high strain-rate tests. Due to the lack of available material, only one tensile specimen was tested at each orientation. Micro-measurements CEA-06-125UT-350 biaxial strain gages were mounted in the center of the gage length of the specimens, with the foil grids arranged parallel and perpendicular to the tensile axis, as shown in Figure 8. Testing was performed on an Instron model 4302 bench-top testing system. The strain gage was balanced before mounting the specimen in the testing machine, and load was applied to the specimen at a constant rate of 0.05 inch/minute until a strain reading of 0.8% was reached and the test was terminated. The permanent residual strain due to

plastic deformation of the test specimen was measured using a Micro-Measurements switch and balance unit, and the strain readings were converted to displacements and used in the calculation of the r-value.

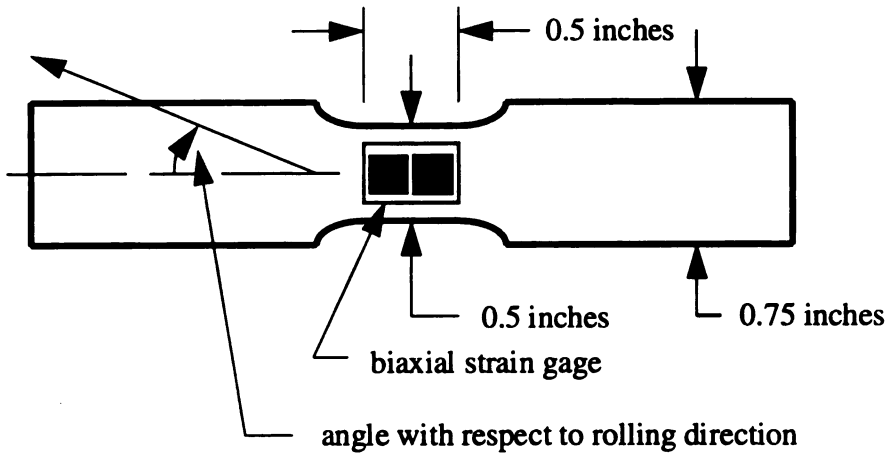

Figure 8: R-value Test Specimen

Three-point bending tests were performed on specimens with orientations of 0, 15, 30, 45, 60, 75 and 90° with respect to the rolling direction, according to ASTM E855-84. The specimens were prepared by shearing rectangular strips of the appropriate size from the sheet steel and removing any burrs along the sheared edges with a file. The tin coating was left intact, assuming that the thickness of the coating would have negligible effect on the flexure strength of the sheet material. The specimen and loading schematic are shown in Figure 9. Flexure testing was performed on an Instron model 4206 universal testing machine. Data collection, stress at yield and flexural modulus calculations were performed using Instron Series IX computer software.

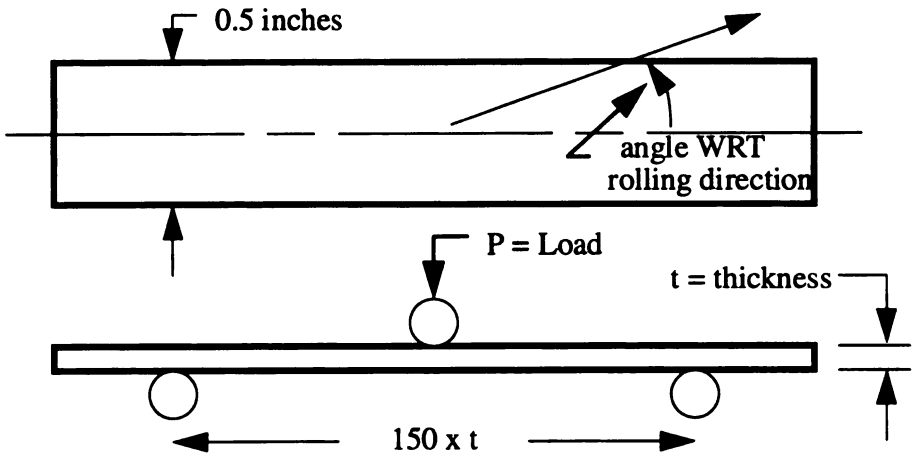

Figure 9: Three-Point Bending Test Specimen and Loading Schematic

Texture Analysis

Pole figure data was collected for 62# and 78# plate using specimens that were sheared from the steel sheet with orientation and dimensions as shown in Figure 10, mechanically ground to remove the tin coating, and polished with 5 μm and 0.05 μm suspensions of Al_2O_3 in distilled water. Measurements of the texture were taken at the surface, as well as grinding the specimen to a reduced thickness and measuring the texture towards the center of the sheet. The pole figure measurements were performed using a Scintag XRD 2000 X-ray diffractometer with Kα radiation in conjunction with a pole figure goniometer, as pictured in Figure 11.

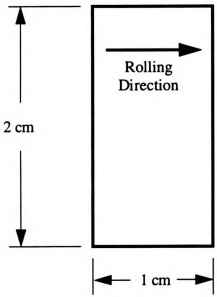

Figure 10: Texture Analysis Specimen

Figure 11: Scintag XRD 2000 X-Ray Diffractometer

The data acquisition system was automated, and consisted of measuring diffracted intensity at background levels on either side of a diffraction peak, and then collecting intensity measurements at the peak angle, with specimen tilt ranging from 0 to 75° at 5° increments and 360° rotation at each tilt angle with 5° increments. Three diffraction peaks were located for each sample by performing a diffraction scan near each peak. A rough approximation for the peak locations was determined using the Powder Diffraction Files compiled by the International Centre for Diffraction Data for α-Fe. The standards book lists d-spacings for {110}, {200} and {211} planes as 2.03, 1.43 and 1.17 Å respectively. The d-spacings were used in conjunction with the wavelength for Kα copper radiation, λ = 1.542 Å, to determine the peak angles with the Bragg equation:

$$\lambda = 2d\sin\Theta$$

where: λ = wavelength of radiation
d = interplanar spacing
Θ = diffraction peak angle

The pole figure raw data was reduced using popLA [22], the preferred orientation package from Los Alamos National Laboratories. Defocusing corrections were made using a theoretical algorithm, rather than an experimental defocusing curve, so the corrections were self-consistent, but not absolute. The data was rotated to allow for misalignment of the specimen, symmetrized, and the outer ring was computed using harmonic analysis. The program was used to generate 110, 200 and 211 pole figures; normal direction, rolling direction and transverse direction inverse pole figures; as well as sample orientation distributions and crystallite orientation distributions. An additional utility program included in the popLA software allows for the conversion of texture components given in generic Miller indices to their appropriate sets of Euler angles, which was used in the interpretation of the texture data.

RESULTS

Microstructural Analysis

Polishing and etching of the double-reduced tinplate steel revealed a fully recrystallized ferritic microstructure, with pancake-shaped grains elongated in the rolling direction. Three-dimensional representations of the microstructure for 62# and 78# plate materials are shown in Figures 12 and 13, respectively. The grains appear equiaxed when viewed normal to the sheet surface and on-edge in the rolling direction, and are elongated in the rolling direction when viewed on-edge perpendicular to the rolling direction, which is typical for heavily rolled, fully recrystallized plate steel. Grain size, aspect ratio and grain volume data collected on the plate steel specimens are listed in Table 2.

Table 2: Microstructural Data

Material	Width (μm)	Height (μm)	Length (μm)	Aspect Ratio	Volume (μm^3)	# Grains Thru Thickness
62# plate	13.6	6.9	25.4	1.97	1248	25
78# plate	10.6	5.9	17.8	1.80	581	37

While the aspect ratio of the two materials is very similar, the grain size of the 62# plate material is larger and the unit grain volume is significantly larger than the 78# plate material. The larger grain size of the 62# plate material translates into a correspondingly lower yield strength and tensile strength. The 62# and 78# plate materials have similar microstructures, both consisting of fully rectrystallized ferrite. Even though the microstructures appear nearly identical, slight differences in the processing parameters

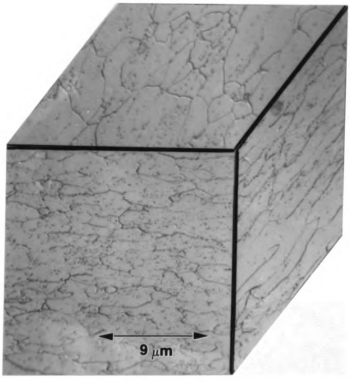

Figure 12: Microstructure of 62# Plate in Width, Height and Thickness Directions

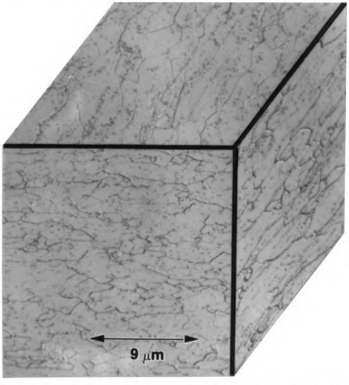

Figure 13: Microstructure of 78# plate in Width, Height and Thickness Directions.

can alter the substructure of the material. However, the difference in thickness between the two plate materials is accounted for in the hot-rolling operation, with both materials experiencing the same amount of cold reduction and additional reduction after annealing. Therefore, the plate materials are expected to have very similar substructures, hence the microscopic substructures of the plate steel was not investigated. The fracture surface morphology of failed tensile test specimens is shown in Figures 14 and 15 for 62# and 78# plate, respectively.

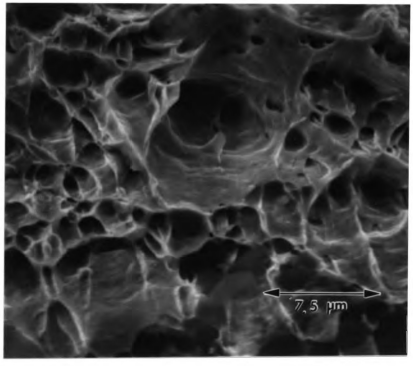

Figure 14: Fracture Surface of 62# Plate Tensile Specimen

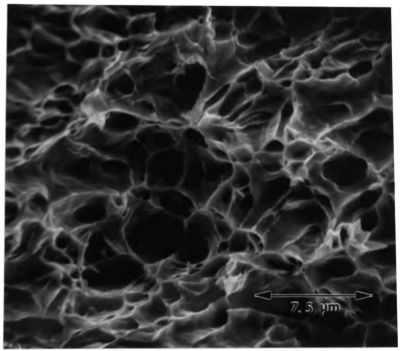

Figure 15: Fracture Surface of 78# Plate Tensile Specimen

The above micrographs clearly show the failure mode as ductile dimple rupture. Specimens with the tensile axis parallel to the rolling direction were photographed, specimens oriented 90° to the rolling direction were also investigated, with identical failure mode.

Mechanical Testing

Results from the standard tensile tests are shown in Tables 3 - 14, with comparison plots of 62# vs. 78# plate materials being shown in Figures 18 - 22. Typical stress-strain curves for the double-reduced tinplate are shown in Figures 16 and 17. As shown in the comparison plots, the offset yield strength and peak strength increase as the angle with respect to the rolling direction varies from 0 to 90°. For the 62# plate and 78# plate

materials, the increase in both yield strength and peak strength is in the range of 14-16% as the tensile axis varies from 0 to 90° with respect to the rolling direction. While both materials show a similar trend in strength, the 78# plate material has a strength 8-10% higher than the 62# plate material.

The Young's modulus remains relatively constant as the angle with respect to the rolling direction varies from 0 to 90°, with values for the 62# and 78# plate materials being very similar. During the tensile testing, a two inch extensometer was used to measure the strain. The standard deviation of the modulus values, listed in Tables 7 and 8, are rather high. The scatter of the measured modulus could be due to several factors, including slippage of the extensometer and factors associated with the thinness of the specimens.

The percent plastic elongation to failure, as shown in Figure 21, shows an opposite trend. As the angle with respect to the rolling direction varies from 0 to 90°, the percent plastic elongation decreases for both materials. The 62# plate material exhibited a higher plastic elongation to failure than the 78# plate material, which is consistent with the lower strength of the 62# plate.

The strain hardening exponent, n, increased as the tensile axis with respect to the rolling direction varied from 0 to 90°. The strain hardening exponent is a measure of the increase in strength of a material due to plastic deformation, and for this study was determined from the yield point to the peak stress range of the stress-strain curve. The strain hardening exponent is the slope of the assumed linear relationship between the logarithm of the true stress and logarithm of true strain.

The angle of fracture with respect to the tensile axis was also measured, with values ranging from 55 - 61° for both 62# and 78# plate materials. Lüders bands have been shown to form in steel specimens at approximately 55° to the stress axis, and were observed during the tensile testing. Eventual failure of the specimen occured at the location of a Lüders band, which would explain the observed angle of fracture.

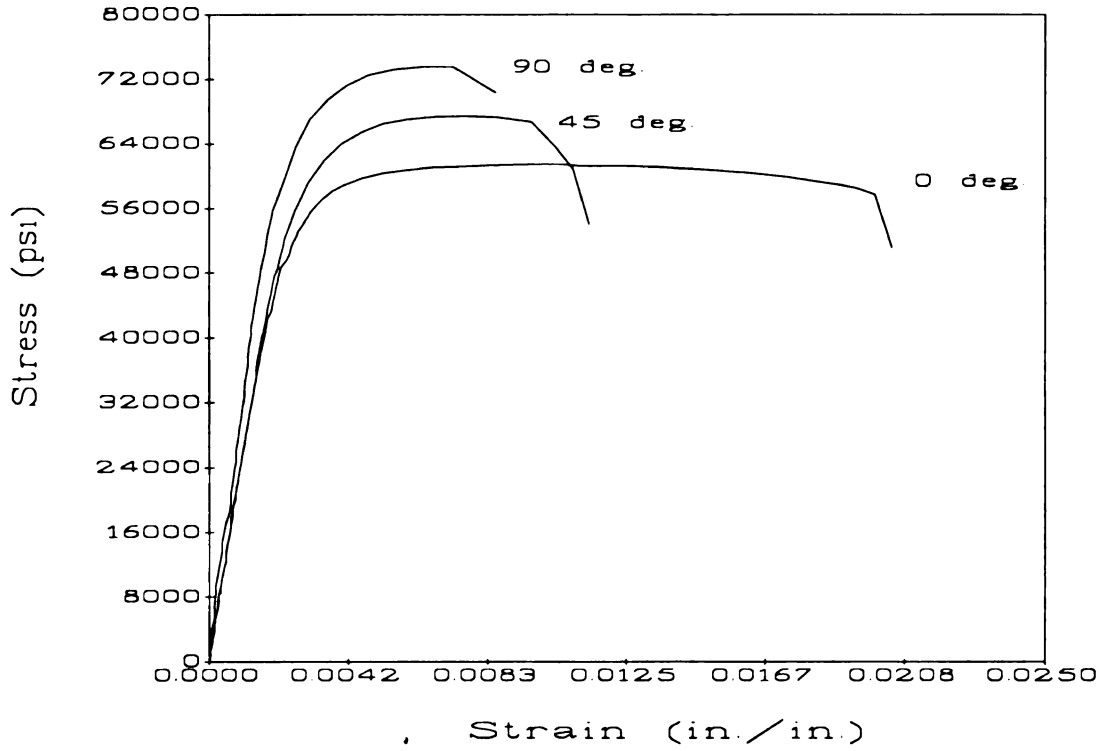

Figure 16: Stress - Strain Curves for 62# Plate Steel

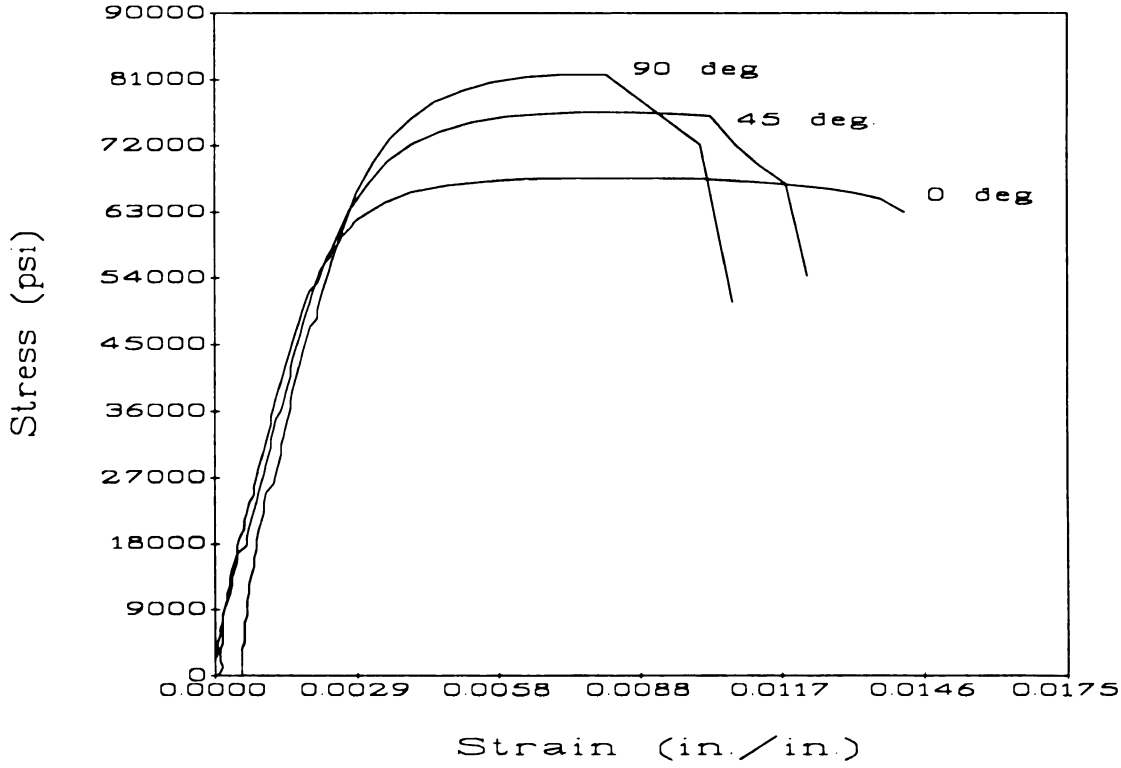

Figure 17: Stress - Strain Curves for 78# Plate Steel

Table 3: 0.2% Offset Yield Strength (psi) -- 62# Plate

Angle/ RD	1	2	3	4	5	Avg.	σ
0	65,450	66,150	64,680	65,040	*	65,330	630
15	65,560	65,690	66,830	64,950	66,580	65,920	771
30	68,190	67,250	68,280	69,160	68,290	68,240	676
45	70,200	69,040	69,870	70,310	70,670	70,020	618
60	72,440	73,210	72,270	73,500	72,510	72,790	539
75	74,720	74,910	75,310	74,980	75,190	75,030	268
90	77,850	77,720	77,710	77,820	*	77,780	71

Table 4: 0.2% Offset Yield Strength (psi) -- 78# Plate

Angle/ RD	1	2	3	4	5	Avg.	σ
0	71,510	72,880	72,560	73,130	*	72,520	713
15	74,470	73,840	74,520	74,190	*	74,260	309
30	75,760	75,180	74,310	75,130	76,490	75,380	810
45	77,580	*	78,200	78,120	77,730	77,910	301
60	78,400	79,660	79,090	80,220	79,950	79,460	725
75	*	83,600	*	83,490	83,750	83,610	129
90	84,590	84,550	84,740	83,540	*	84,350	546

Table 5: Peak Stress (psi) -- 62# Plate

Angle/ RD	1	2	3	4	5	Avg.	σ
0°	67,690	68,180	67,160	67,220	*	67,560	474
15°	67,880	68,370	68,100	68,230	68,590	68,230	269
30°	69,850	69,860	71,000	70,690	70,390	70,360	508
45°	72,100	72,800	72,240	72,930	72,780	72,570	373
60°	74,450	74,800	73,900	74,710	74,790	74,530	382
75°	76,530	76,350	76,590	76,530	76,590	76,520	112
90°	80,220	80,050	79,950	79,700	*	79,980	217

Table 6: Peak Stress (psi) -- 78# Plate

Angle/ RD	1	2	3	4	5	Avg.	σ
0°	74,630	74,220	74,480	74,070	*	74,350	252
15°	76,680	75,560	75,820	76,320	*	76,100	504
30°	77,470	77,270	77,550	77,570	77,640	77,500	142
45°	79,870	*	79,630	79,900	80,060	79,860	181
60°	81,720	82,060	81,790	82,120	82,050	81,950	178
75°	*	86,470	*	86,130	86,310	86,310	166
90°	86,780	86,690	86,740	86,830	*	86,760	56

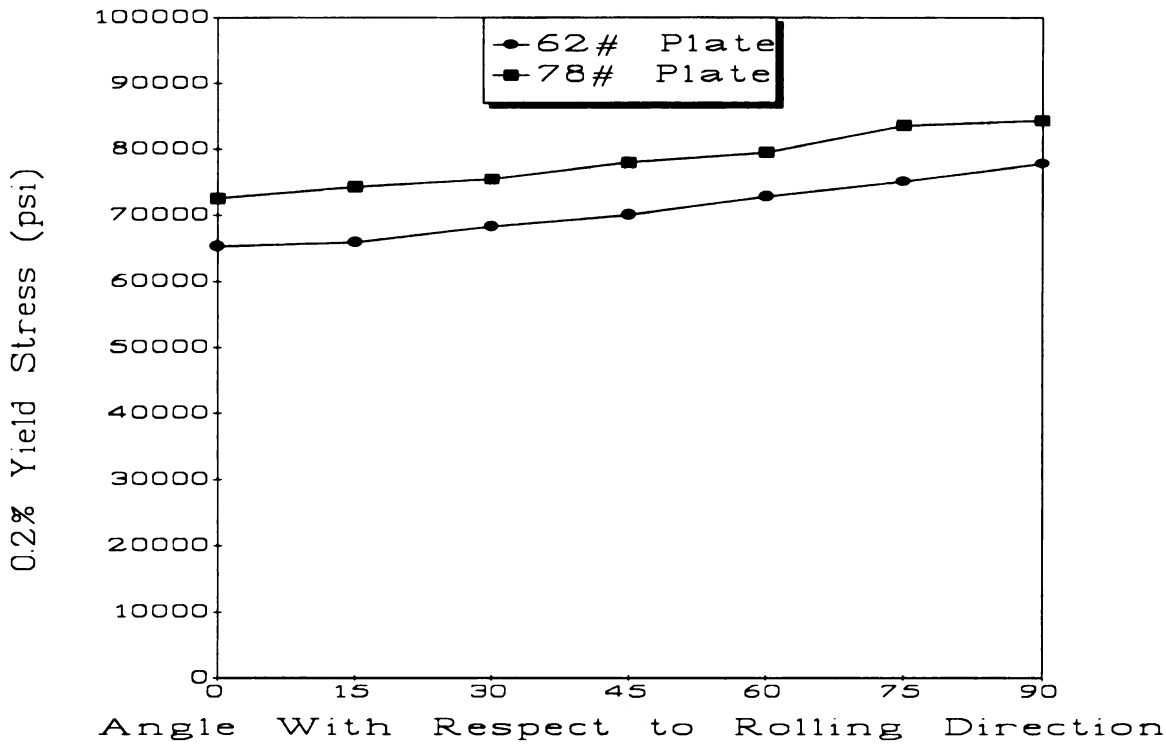

Figure 18: 0.2% Yield Stress

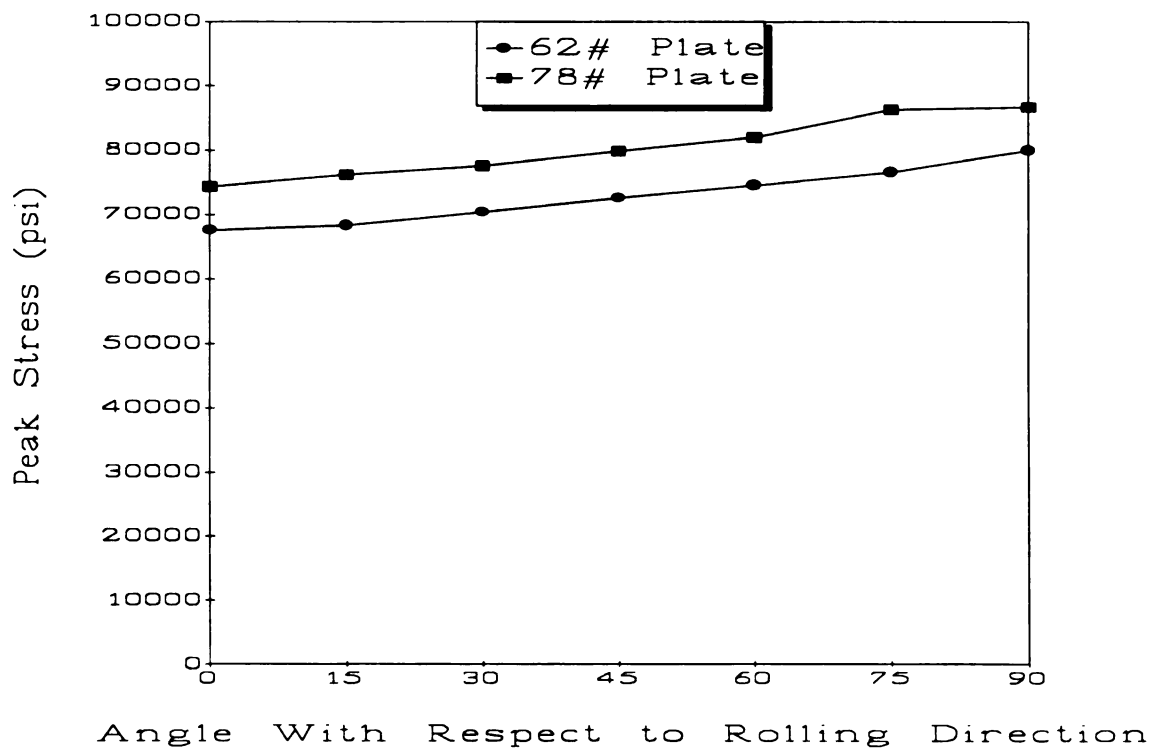

Figure 19: Peak Stress

Table 7: Young's Modulus (ksi) -- 62# Plate

Angle/ RD	1	2	3	4	5	Avg.	σ
0°	26,400	27,770	27,120	27,600	*	27,220	613
15°	26,890	27,450	24,550	25,600	25,060	25,910	1,224
30°	25,370	30,250	27,420	27,320	27,580	27,640	1,844
45°	29,280	31,650	28,390	28,960	28,410	29,340	1,348
60°	28,990	29,040	31,040	29,930	28,320	29,460	1,049
75°	28,970	26,880	29,450	27,440	27,730	28,260	1,171
90°	31,620	34,250	33,240	29,980	*	32,270	1,872

Table 8: Young's Modulus (ksi) -- 78# Plate

Angle/ RD	1	2	3	4	5	Avg.	σ
0°	31,140	*	29,500	26,770	*	29,137	2,208
15°	31,690	29,720	28,110	27,980	*	29,370	1,733
30°	29,190	29,960	36,530	32,950	26,440	31,010	3,858
45°	27,990	*	29,130	27,520	31,750	29,100	1,894
60°	28,890	27,470	28,370	28,860	30,790	28,880	1,214
75°	*	30,140	*	29,680	30,810	30,210	569
90°	32,070	30,540	29,880	29,310	*	30,450	1,191

Table 9: Percent Plastic Elongation -- 62# Plate

Angle/ RD	1	2	3	4	5	Avg.	σ
0°	2.044	1.973	1.900	2.176	*	2.023	0.117
15°	1.453	1.548	1.538	1.399	1.511	1.490	0.063
30°	1.129	1.143	1.121	*	1.209	1.150	0.040
45°	1.235	1.061	1.072	0.948	1.030	1.069	0.105
60°	0.896	1.152	0.831	0.904	0.821	0.921	0.135
75°	0.915	0.862	0.897	0.892	0.837	0.878	0.035
90°	0.836	0.861	0.896	0.584	*	0.794	0.143

Table 10: Percent Plastic Elongation -- 78# Plate

Angle/ RD	1	2	3	4	5	Avg.	σ
0°	1.571	1.369	1.598	1.495	*	1.508	0.102
15°	1.145	1.070	1.308	1.206	*	1.182	0.100
30°	0.932	0.984	1.091	1.052	0.992	1.010	0.062
45°	0.941	*	0.886	1.017	0.878	0.931	0.064
60°	0.865	0.858	0.945	0.876	0.888	0.886	0.035
75°	*	0.895	*	0.842	0.854	0.864	0.028
90°	0.870	0.892	0.933	0.902	*	0.899	0.026

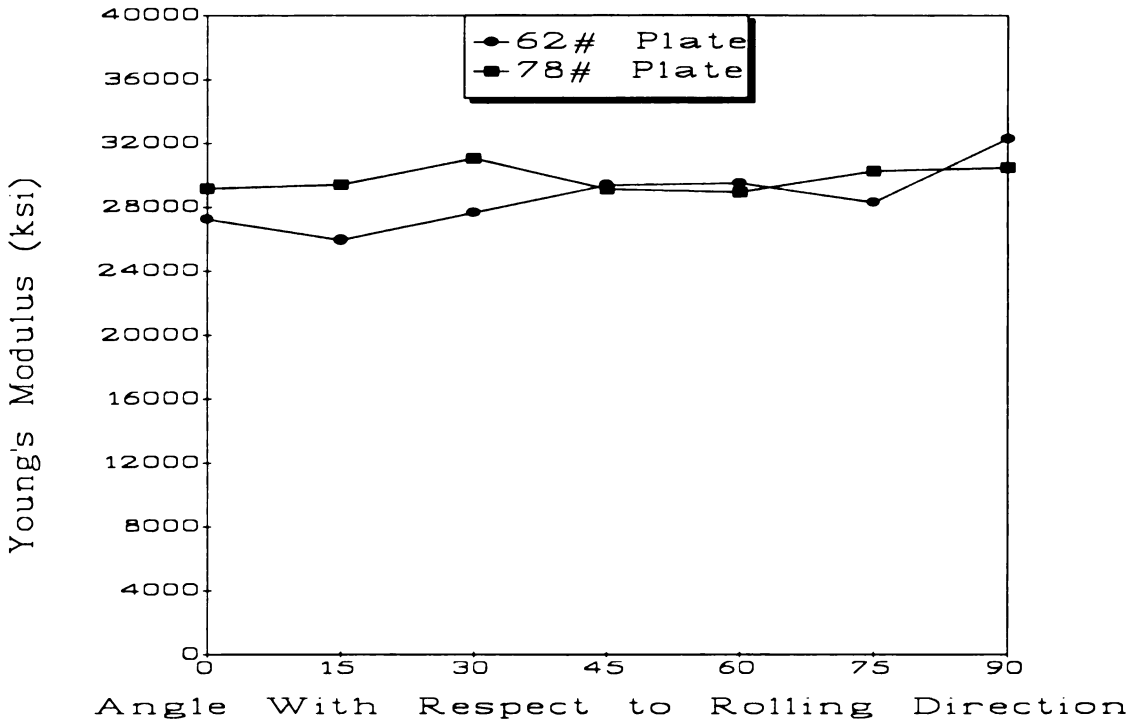

Figure 20: Young's Modulus

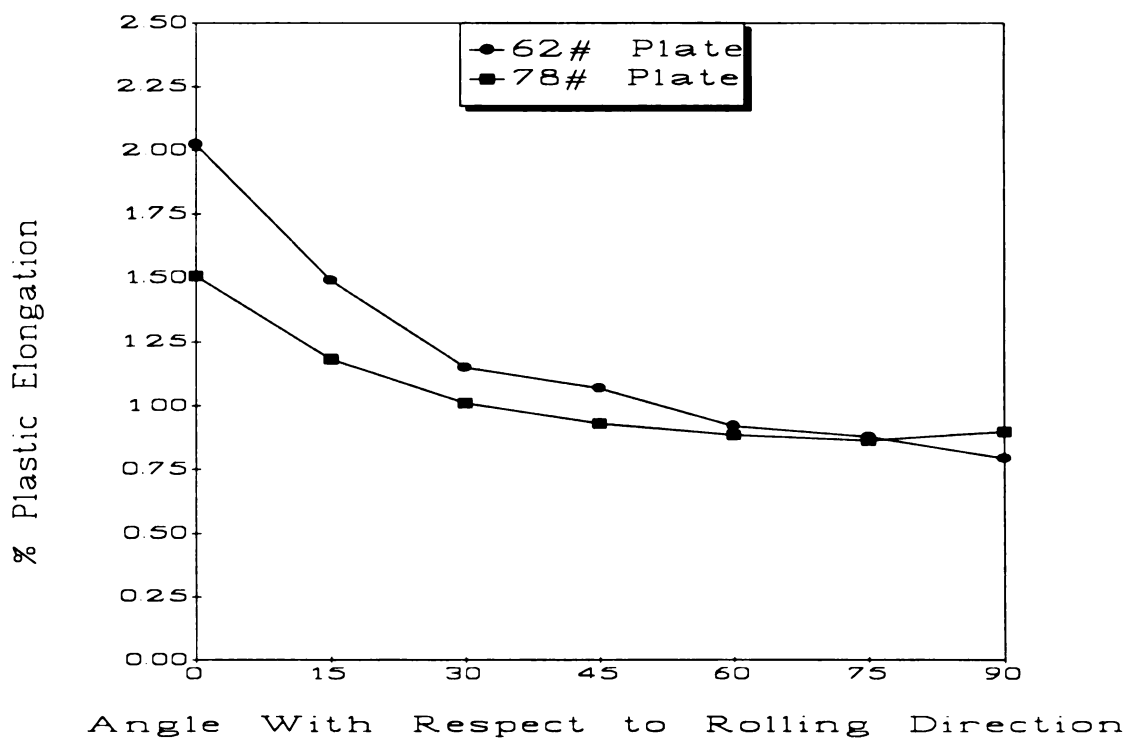

Figure 21: Percent Plastic Elongation

Table 11: Strain Hardening Exponent, n -- 62# Plate

Angle/RD	1	2	3	4	5	Avg.
0°	0.2230	0.2304	0.2315	0.2170	0.2063	0.2216
15°	0.2285	0.2293	0.2376	0.2696	0.2781	0.2486
30°	0.2593	0.2402	0.2602	0.2540	0.2931	0.2614
45°	0.2218	0.2694	0.2867	0.2860	0.2890	0.2706
60°	0.3025	0.2748	0.2547	0.3002	0.2954	0.2855
75°	0.2770	0.3303	0.3016	0.2918	0.2482	0.2898
90°	0.2698	0.2556	0.2759	0.3021	0.2648	0.2736

Table 12: Strain Hardening Exponent, n -- 78# Plate

Angle/RD	1	2	3	4	5	Avg.
0°	0.2953	0.2079	0.2424	0.2790	0.2163	0.2482
15°	0.2895	0.3100	0.2874	0.3030	0.2770	0.2934
30°	0.2784	0.3214	0.3399	0.2866	0.3056	0.3064
45°	0.3042	0.2905	0.3075	0.2935	0.3226	0.3037
60°	0.3335	0.3190	0.3405	0.3054	0.3246	0.3246
75°	0.3193	0.2765	0.3266	0.3005	0.3356	0.3117
90°	0.3003	0.3510	0.3225	0.3214	0.3604	0.3311

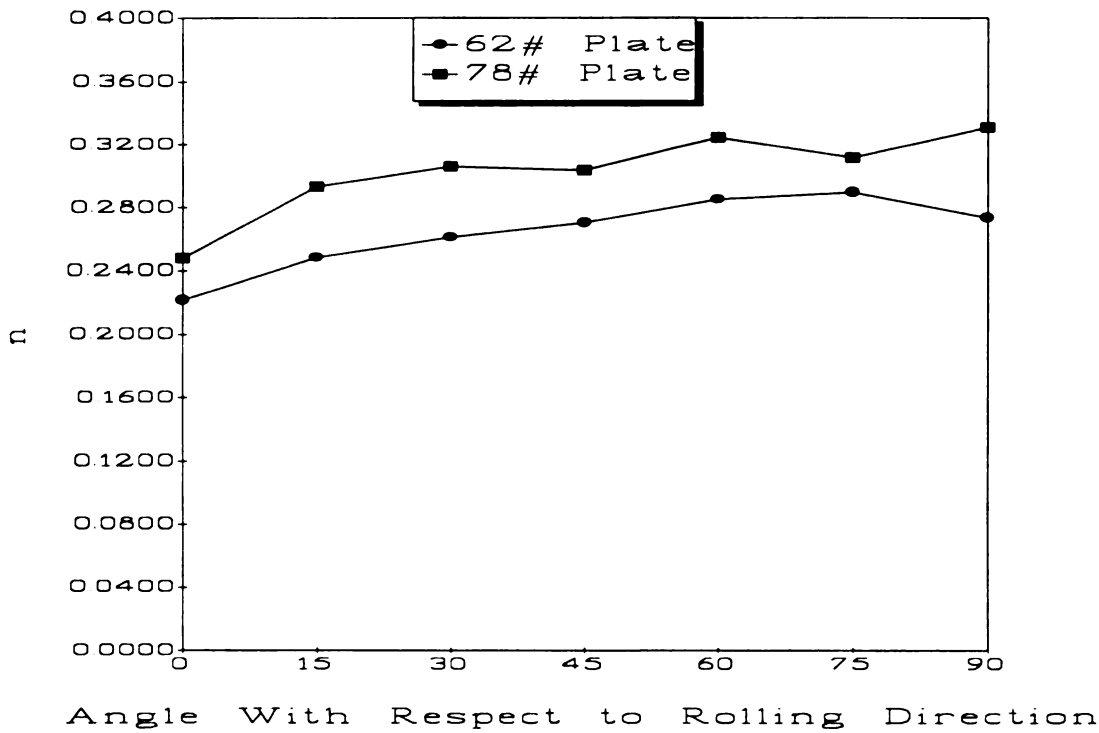

Figure 22: Strain Hardening Exponent, n

Table 13: Angle of Fracture With Respect to Specimen Axis -- 62# Plate

Angle/RD	1	2	3	4	5	Avg.
0°	61°	57°	61°	60°	*	60°
15°	60°	58°	61°	59°	58°	59°
30°	58°	55°	60°	59°	57°	58°
45°	52°	51°	58°	56°°	57°	55°
60°	51°	50°	57°	50°	58°	53°
75°	52°	53°	52°	51°	58°	53°
90°	55°	55°	53°	55°	*	55°

Table 14: Angle of Fracture With Respect to Specimen Axis (degrees) -- 78# Plate

Angle/RD	1	2	3	4	5	Avg.
0°	60°	62°	61°	60°	*	61°
15°	58°	59°	58°	57°	59°	58°
30°	55°	57°	56°	55°	54°	55°
45°	57°	51°	58°	51°	56°	55°
60°	57°	57°	55°	57°	58°	57°
75°	59°	55°	55°	55°	55°	56°
90°	54°	52°	54°	53°	54°	53°

High strain-rate tensile results are given in Table 15 and Figure 23. The values listed are an average of two specimens. Some difficulties were experienced during the high strain-rate testing. A hydraulic leak existed on the MTS testing machine between the servovalve and the actuator assembly at the time the testing was performed, which lead to several problems. The targeted strain rate of 1×10^2 sec^{-1} was unachievable, with the actual strain rate of the test being approximately 1×10^1 sec^{-1}. As the strain rate of the test was increased, the amount of displacement achieved by the actuator (crosshead) decreased. Therefore, the strain rate had to be compromised in order to develop enough crosshead displacement to plastically deform the test specimen. While the test specimens showed signs of permanent deformation (Lüders bands), the peak stress values listed in Table 15 seem inexplicably low. One would expect the flow stress of the material to increase at high strain-rates because the ability of the material to recover dynamically lags behind the rate of strain hardening. However, the peak stress results obtained during this study are significantly lower than those measured during the standard tensile tests, which may be due to the lack of sufficient crosshead travel during the test. Even though the values appear low, the trend of increased strength as the angle with respect to rolling direction increases remains intact.

Table 15: High Strain-Rate Testing -- Peak Stress (psi)

Material	0°	15°	30°	45°	60°	75°	90°
62# plate	38,509	40,800	40,697	40,800	43,541	45,333	45,799
78# plate	43,514	43,472	44,411	44,342	45,521	46,775	48,682

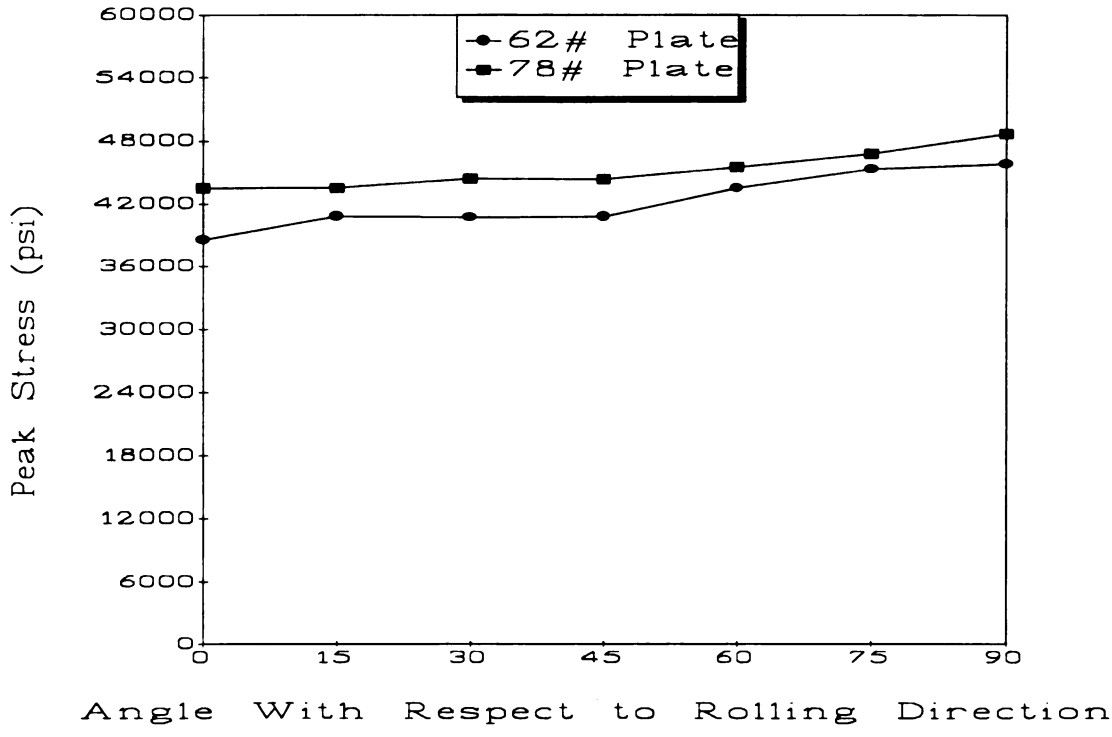

Figure 23: High Strain-Rate Test Results

Results from the r-value testing are given in Table 16. As seen from the data, several problems were encountered during the testing. In order to obtain an accurate reading of the permanent plastic deformation encountered by the test specimen, the bond between the strain gage and the test specimen must be very strong. Several of the strain gages had very poor bonds to the test specimens, which was discovered after the testing was complete. Another problem was in the geometry of the test specimens used. The ASTM test method specifies a 2 inch gage length test specimen, allowing for very uniform strain in the gage section. Due to the lack of available material, 0.5 inch gage length specimens had to be used. While the strain in the gage section may have been fairly uniform through most of the test, the final strain of 0.8% caused the formation of Lüders bands in specimens approaching 90° with respect to the rolling direction. These Lüders bands, whether they fall in the area of the strain gage or not, have a significant impact on the test results.

Table 16: R-Value Testing Results

Material	0°	15°	30°	45°	60°	75°	90°
62 # plate	0.489	0.982	0.530	0.830	*	0.445	0.904
78# plate	0.340	*	0.422	1.610	1.440	*	*

Flexure testing results are shown in Tables 17-20 and Figures 24 and 25. Results from the three-point bending tests show the same trend as the standard tensile tests, an increase in strength as the angle with respect to the rolling direction increases from 0 to 90°. The yield stress increases approximately 30% from 0 to 90° for the 62# plate steel, and 20% for the 78# plate steel. Parallel to the rolling direction, the 78# plate steel has a strength 18% higher than the the 62# plate steel, and transverse to the rolling direction the strength is 5% higher than the 62# plate material. As would be expected, the flexural modulus also increases as the angle with respect to the rolling direction increases. The 62# plate exhibited a 20% increase in modulus, with the 78# plate material exhibiting a 9% increase. The modulus at 0° was 10% higher for the 78# plate, and almost equal at 90°.

Table 17: Stress At Yield (psi) -- 62# Plate

Angle/RD	1	2	3	4	Average	σ
0	91,070	*	98,690	98,520	96,090	4352
15	100,700	101,400	98,840	100,300	100,300	1068
30	112,700	110,200	112,500	116,100	112,900	2452
45	122,800	120,800	122,300	122,800	122,200	941
60	127,800	128,300	131,800	130,200	129,500	1814
75	131,000	138,100	138,500	132,800	135,100	3767
90	137,200	134,500	141,300	141,000	138,500	3254

Table 18: Stress At Yield (psi) -- 78# Plate

Angle/RD	1	2	3	4	Average	σ
0	116,900	116,700	115,900	116,600	116,500	428
15	121,400	123,200	121,000	121,800	121,900	968
30	128,700	128,300	128,600	129,600	128,800	542
45	133,600	134,200	132,800	134,800	133,800	835
60	136,700	138,200	139,200	142,200	139,100	2346
75	141,800	145,100	141,300	143,300	142,900	1695
90	146,700	146,700	146,600	146,500	146,600	116

Table 19: Flexural Modulus (ksi) -- 62# Plate

Angle/RD	1	2	3	4	Average	σ
0	26,810	*	25,990	29,370	27,390	1763
15	28,190	28,880	26,370	25,650	27,270	1514
30	28,530	25,800	28,310	31,150	28,450	2184
45	27,800	27,590	27,900	28,530	27,960	4015
60	32,920	30,180	29,950	31,330	31,090	1355
75	30,430	34,080	32,020	31,760	32,070	1510
90	35,130	32,650	33,630	32,870	33,570	1121

Table 20: Flexural Modulus (ksi) -- 78# Plate

Angle/RD	1	2	3	4	Average	σ
0	31,900	30,080	29,610	30,190	30,440	1003
15	35,170	31,450	30,010	39,040	31,420	2689
30	30,790	30,990	32,550	29,400	30,930	1289
45	31,730	29,510	31,420	31,080	30,930	985
60	30,670	31,140	32,440	32,010	31,570	804
75	31,030	33,420	34,240	32,940	32,910	1364
90	33,280	33,160	33,470	32,740	33,160	309

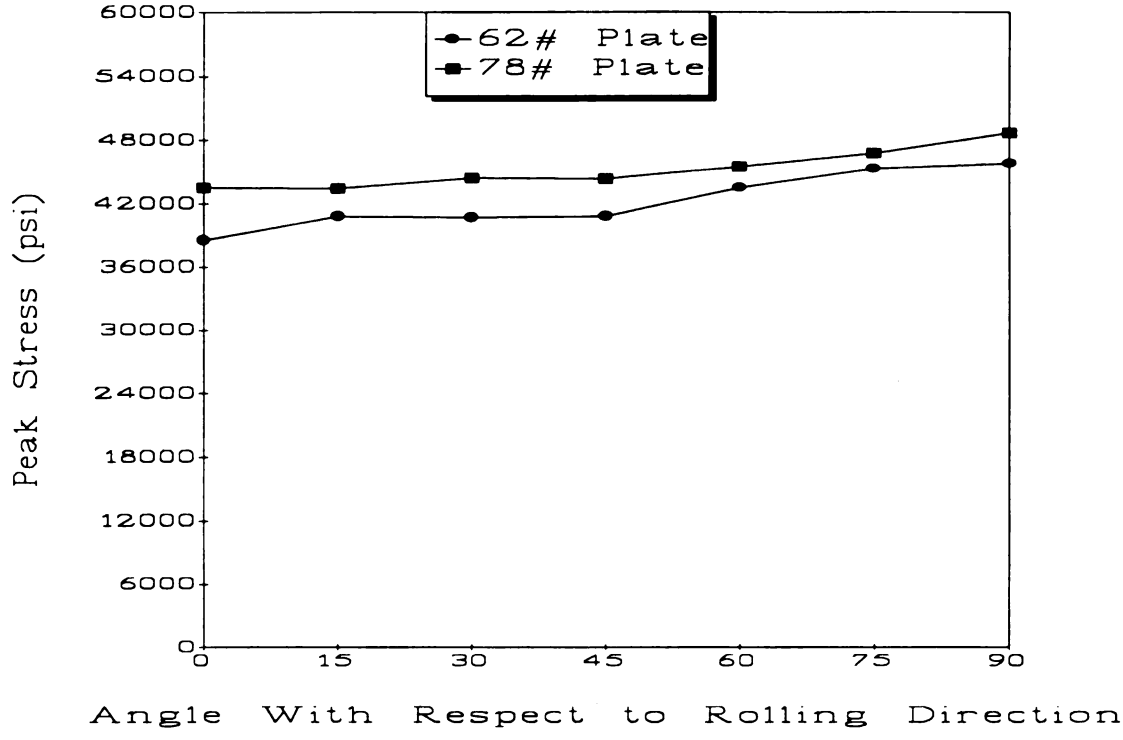

Figure 24: Flexure Stress at Yield

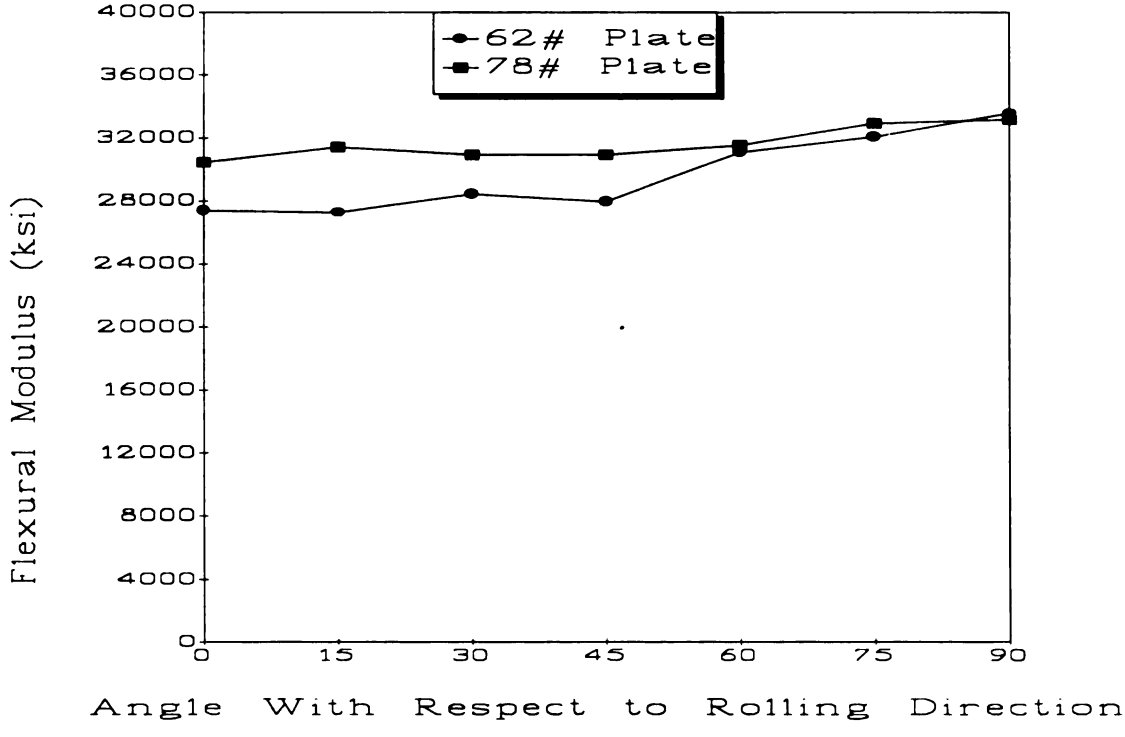

Figure 25: Flexural Modulus

Texture Analysis

The pole figure diffraction data was input into the popLA software package, and pole figures, inverse pole figures, sample orientation and crystallite orientation distributions were generated for samples of 62# plate and 78# plate. (110), (200) and (211) pole figures for the 62# and 78# plate materials are shown in Figures 27 and 28, respectively. A pole figure is a stereographic projection showing the density of particular crystallographic poles as a function of orientation, with the sample axes (normal, rolling and transverse directions) as a reference frame. Pole figures are often very difficult to interpret. Textures of rolled sheets are usually given in terms of ideal orientations, such as $\{111\}\langle 01\bar{1}\rangle$. However, an experimentally measured pole figure is quite complex, exhibiting multi-component textures. The actual texture is commonly described as having a "spread" of orientations from one texture component to one or several other texture components. The (110) and (200) pole figures are typical of severely rolled low-carbon sheet steel. The (200) pole figures reveal two major orientation spreads. The strongest component is a fiber texture with a <111> fiber axis parallel to the normal direction, with an orientation spread from $\{111\}\langle 01\bar{1}\rangle$ to $\{111\}\langle 11\bar{2}\rangle$. A partial fiber also exists, with the <110> direction parallel to the rolling direction and an orientation spread from $\{001\}\langle 110\rangle$ to $\{111\}\langle 1\bar{1}0\rangle$, as shown in Figure 26

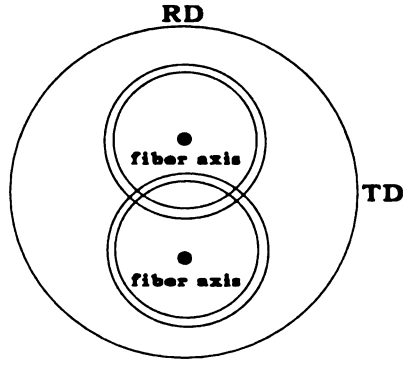

Figure 26: (100) Pole Figure Showing <110> Fiber Texture [23]

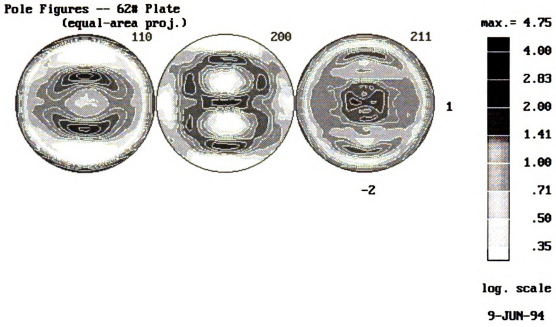

Figure 27: Pole Figures -- 62# Plate

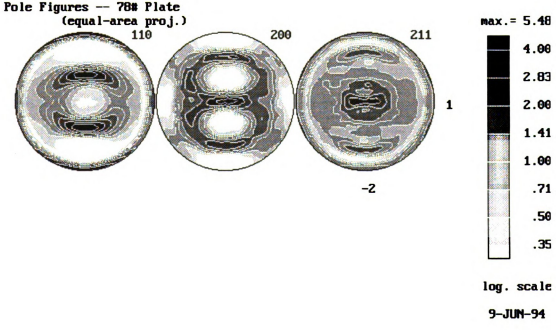

Figure 28: Pole Figures -- 78# Plate

Inverse pole figures in the normal, rolling and transverse directions for the 62# and 78# plate materials are shown in Figures 29 and 30, respectively. Inverse pole figures are most useful for the interpretation of true fiber textures, such as those produced by wire drawing. Since these figures do not indicate rotations that may occur around the chosen axis, they are less useful for materials which have undergone a deformation process of less symmetry, such as rolling. The figure uses one quadrant of the standard 001 stereographic projection as a reference frame, and displays intensity contours corresponding to the frequency with which the various directions in the crystal coincide with the specimen axis under consideration. As for the pole figure data, the textures present in the 62# and 78# plate materials are very similar. The normal direction inverse pole figure indicates a very strong intensity of <111> directions parallel to the normal direction of the sample. This indicates that a high density of {111} planes are parallel to the surface of the sheet, which is consistent with the {111}<uvw> fiber texture mentioned previously. The rolling direction inverse pole figure shows a high intensity of <011>, with a smaller intensity associated with <112>. The {111}<uvw> fiber texture consists of an orientation spread from $\{111\}\langle\bar{1}10\rangle$ to $\{111\}\langle 11\bar{2}\rangle$, which is consistent with the results obtained from the inverse pole figures. The transverse direction inverse pole figure also shows intensity peaks located at <011> and <112>. The intensities associated with the transverse direction inverse pole figure are lower than those for the rolling direction, which is logical since the deformation occurs in the rolling direction, and the directions should be more strongly aligned due to the symmetry of the process. The location of the intensity peaks is also expected since since the $\langle\bar{1}10\rangle$ and $\langle 11\bar{2}\rangle$ directions are orthogonal, and the rolling and transverse directions are also orthogonal.

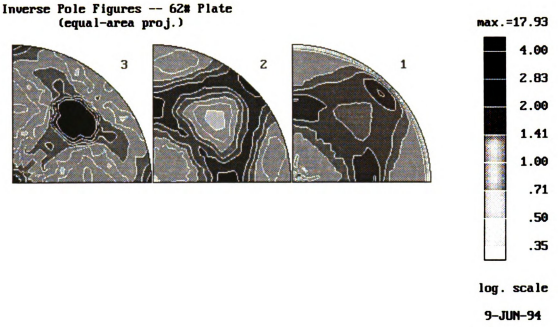

Figure 29: Inverse Pole Figures -- 62# Plate

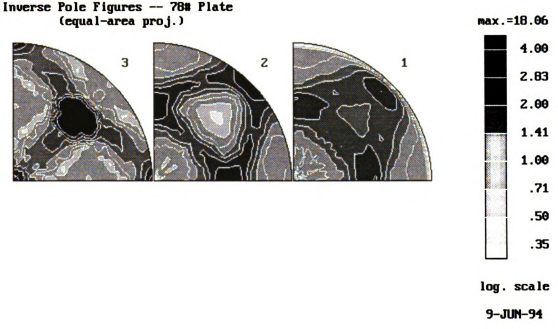

Figure 30: Inverse Pole Figures -- 78# Plate

Pole figures and inverse pole figures can yield satisfactory qualitative descriptions of the texture present in a sample, however, sample and crystallite orientation distribution plots are much more descriptive and can yield quantitative results. The problem with pole figures and inverse pole figures is that a general crystallographic orientation has three degrees of freedom, whereas pole figures and inverse pole figures specify only two degrees of freedom. Therefore, pole figures and inverse pole figures are merely "projections" of the three dimensional orientation distribution function, which is the full description of the texture. The three degrees of freedom associated with a crystallographic orientation correspond to three Euler angles, which relate the crystallographic coordinate system (001, 010 and 100) to the sample coordinate system (rolling direction, transverse direction and normal direction). Since three independent parameters are associated with the relation of two orthogonal coordinate systems, the Euler angles are considered to represent three orthogonal axes which define a volume of orientation space [23]. The definition of the Euler angles, and the symbols which represent these angles, varies among several different conventions developed by workers in the field of texture analysis. The method used in this study was the Kocks convention [22], with Euler angles Ψ, Θ and ϕ, as shown in Figure 31.

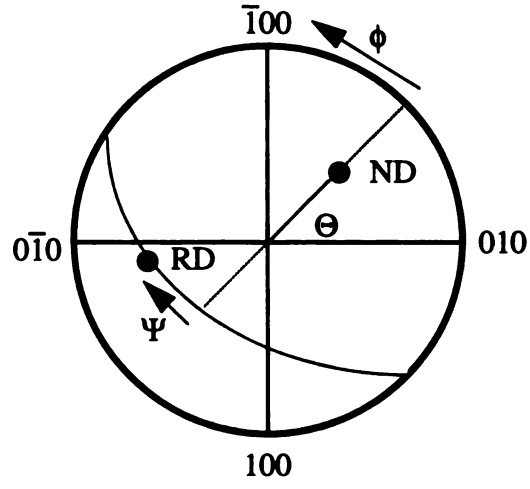

Figure 31: Definition of Kock's Convention Euler Angles [23]

The orientation distribution function (ODF) can be calculated using numerical data obtained from several pole figures by a number of different methods. The most common methods of ODF determination involve either an iterative least squares solution or generalized spherical harmonics. The method used by the popLA software package is the WIMV analysis method. The WIMV method involves the use of the most constructive elements of William's [24] and Imhof's [25] least squares ODF reproduction method, as well as the automatic ghost correction suggested by Matthies and Vinel [26], hence the name WIMV [27]. The analysis procedure involves the creation of "pointers" (or "vectors" or "matrices") which connect each cell in three-dimensional orientation space with all cells on the various pole figures into which they project [22]. The pole figure data is stored on a 5° x 5° grid, with one intensity value associated with each grid cell. The orientation distribution (OD) is calculated on a 5° x 5° x 5° three-dimensional grid in orientation space, with one intensity value associated with each grid cell. A set of "pointers" is established which relate each cell in the OD to the cell or cells of the pole figures into which they project. In general, each OD cell points to several pole figure cells, and each pole figure cell is pointed to by several OD cells. An initial estimate of the OD is calculated by assigning to the OD cell the geometric mean of the intensity values in the pole figure cells to which it points [22]. The estimated OD is then used to recalculate the pole figures, which is essentially done by reversing the process used to estimate the OD. The recalculated pole figures usually do not correspond well with the measured pole figures due to the averaging of intensities in the OD grid cells. Therefore, the ratios of the measured to the recalculated intensity values are averaged and used to calculate a correction factor for each corresponding cell in the OD grid. This procedure is repeated until the solution converges to a stable value. Once a solution to the OD has been obtained, the symmetry between the sample and crystal coordinate systems allows for two equivalent descriptions of the orientation relationship: the sample orientation in terms of the crystal reference frame (sample orientation distribution (SOD)); or the crystal

orientation in terms of the sample reference frame (crystallite orientation distribution (COD)). Since these three-dimensional plots are very difficult to generate and interpret, the orientation distributions are usually presented as a series of parallel sections through orientation space. The SOD has constant Ψ sections, with Θ and ϕ varying from 0 to 90° in each section, while the COD has constant ϕ sections, with Ψ and Θ varying from 0 to 90° in each section, as shown in Figure 32.

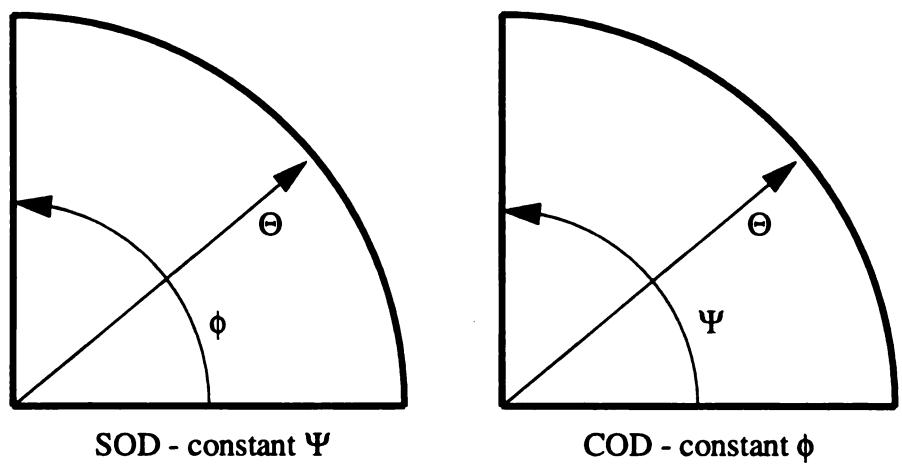

Figure 32: SOD and COD Angle Conventions

Traditionally, each orientation distribution section is plotted in Cartesian coordinates, yielding a square plot in which equal areas on the plot do not represent equal volumes in orientation space. The method of representing orientation distributions employed by the popLA software package plots each section in polar coordinates, projecting densities in each section in an equal-area projection. This method of representation has several advantages over the traditional square plots: equal volumes in orientation space correspond to equal areas in the plot; crystal and sample symmetries are clearly displayed, often allowing for quadrant or hemispherical representations; angles can be directly measured from the plot through the use of a net; and the sum of all sections, or the

projection, is the normal direction inverse pole figure in the case of the SOD, or the (100) pole figure in the case of the COD [28]. The SOD's for the 62# and 78# plate materials are shown in Figures 33 and 34, respectively. As was the case for the pole figures and inverse pole figures, the preferred orientation displayed by the SOD's is very similar for the two plate materials, and the projection is , in fact, the normal direction inverse pole figure. The method used to analyze the SOD's, as well as the COD's, involved the use of a utility program included with the popLA software package, hkl2eul. This program allows the user to input Miller indices in the form (hkl)[uvw], and converts these indices into sets of Euler angles. The listing of Euler angles includes both positive and negative angles from 0 to 360°. Typical rolling and recrystallization textures for steel were input into the program, and the set of Euler angles was pared down to include only positive angles between 0 and 90°, since the SOD sections are quadrants with angles of the same range, and are listed in Table 21. Due to the crystal symmetry involved, indices of lower symmetry require a larger number of Euler angle sets to completely define all equivalent orientations. Comparing the angles listed in Table 21 with the SOD's, the most significant texture component present in the plate steel samples is the $(111)[1\bar{1}0]$ cube-on-corner textures. However, each SOD section shows a significant intensity associated with $\Theta = 55°$ and $\phi = 45°$, indicating a $\{111\}\langle uvw\rangle$ fiber texture with orientation spreads from $\{111\}\langle 1\bar{1}0\rangle$ to $\{111\}\langle \bar{2}11\rangle$. In order to compare the the relative strength of the fiber textures associated with the plate steel materials, the relative intensity (in arbitrary units) at $\Theta = 55°$ and $\phi = 45°$ obtained from the SOD data files was plotted for each section as Ψ ranged from 0 to 90°. This skeleton line associated with the γ-fiber texture for the 62# and 78# plate materials is shown in Figure 35. The peak locations for the 62# and 78# plate materials occur in approximately the same location, with the intensity associated with the 62# plate being higher than that for the 78# plate. The increased intensity is due to the additional grain growth experienced by the thinner material during the annealing cycle. During the grain growth process, the more favorably oriented $\{111\}\langle 1\bar{1}0\rangle$ grains grow

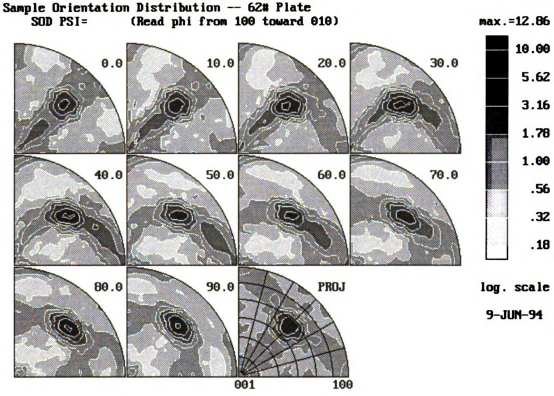

Figure 33: SOD -- 62# Plate

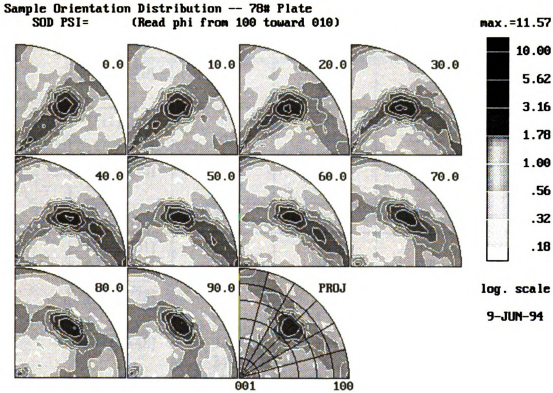

Figure 34: SOD -- 78# Plate

Table 21: Miller Indices and Their Respective Sets of Euler Angles

Orientation	Ψ	Θ	ϕ
$(111)[1\bar{1}0]$	30° 90°	55° 55°	45° 45°
$(111)[\bar{2}11]$	0° 60°	55° 55°	45° 45°
$(112)[\bar{1}10]$	39° 90°	66° 35°	63° 45°
(100)[011]	0°	0°	45°
(100)[001]	0° 0°	0° 0°	0° 90°
$(554)[\overline{22}5]$	0° 64°	60° 52°	45° 51°
$(411)[\overline{14}8]$	23° 24° 70°	19° 76° 76°	45° 14° 14°

at the expense of the less favorably oriented grains, which sharpens the resulting texture. Continued annealing would lead to additional grain growth, and a continued sharpening of the resultant texture.

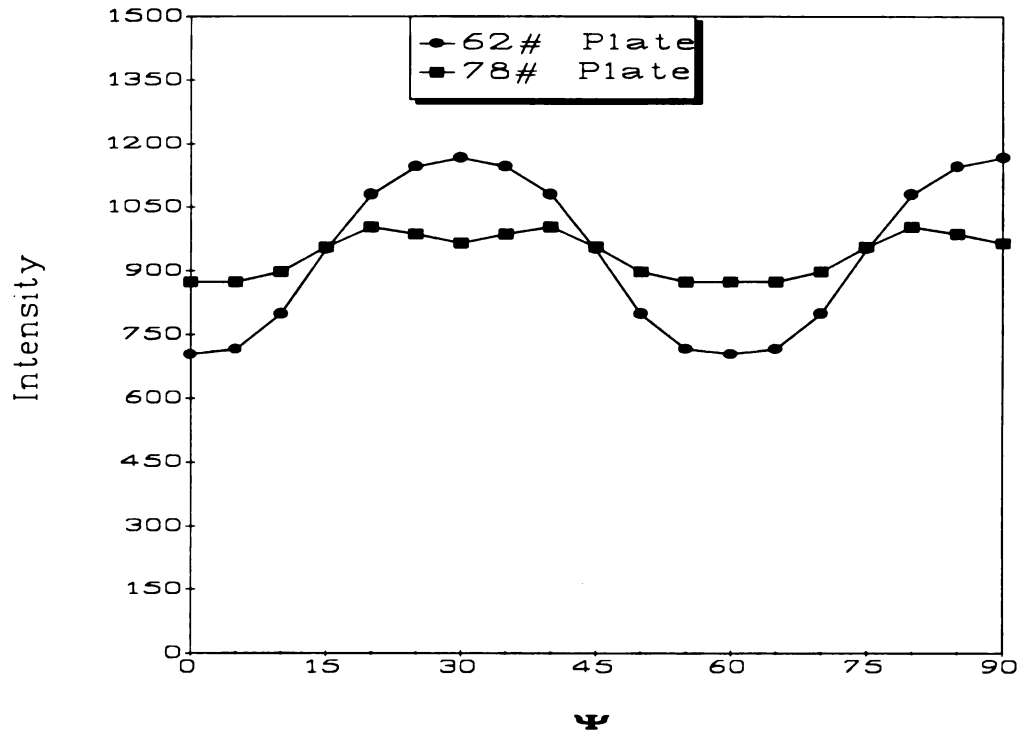

Figure 35: γ - Fiber Skeleton Line

The COD's for the 62# and 78# plate materials are shown in Figures 36 and 37, respectively. Again, the orientation distributions for the two materials are very similar, and the projection of the COD is very similar to the (200) pole figure. Comparing the COD plots with the Euler angles listed in Table 21, it is clear that the predominant texture component is the (111)[$1\bar{1}0$] cube-on-corner orientation, and the intensity maxima located in the $\phi = 45°$ section at $\Theta = 55°$ is indicative of the {111}<uvw> complete fiber texture present in the samples. This location of intensity maxima is the same as that shown in the skeleton line plot of Figure 35, viewed from another direction.

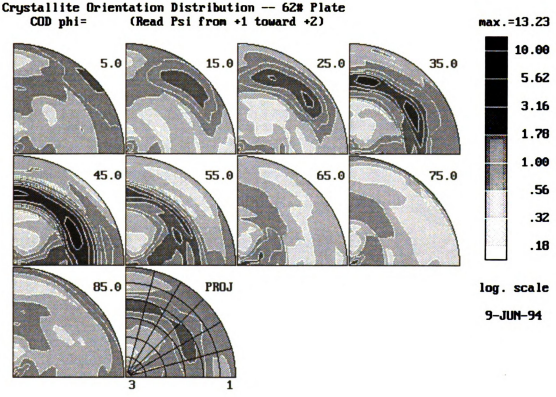

Figure 36: COD -- 62# Plate

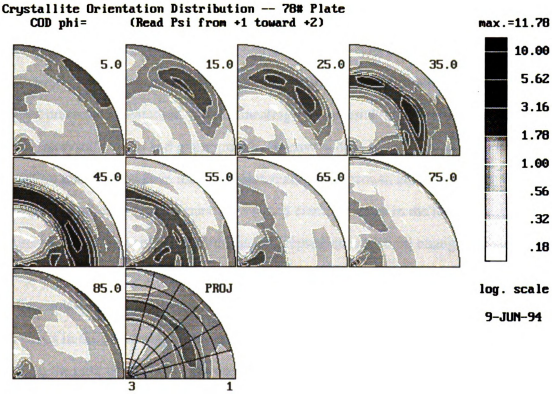

Figure 37: COD – 78# Plate

DISCUSSION

The common metals of industrial importance are polycrystalline aggregates in which each of the individual grains has an orientation that differs from those of its neighbors. During the manufacture of products such as sheet steel, processes such as rolling cause rotations of the crystallites as a result of the shape change and the geometrical constraints due to the imposed stress system. The nature of these rotations is based on the crystallographic nature of the deformation process of slip. The restricted number of slip systems available produce rotations towards a limited number of stable end points, creating a preferred orientation. Upon annealing, the material undergoes the processes of recovery, recrystallization and grain growth. Recovery does not generally affect the deformation texture, however, recrystallization and grain growth are characterized by the movement of high-angle grain boundaries which create changes in the local orientation. The summation of all local orientation changes represents a textural change in the material, which is related to the deformation texture. The existence of sharp crystallographic textures creates pronounced directionality of properties. The anisotropy which exists in the polycrystal is based on the directionality which exists in the single crystal. In the case of bcc α-Fe, the strength is highest along the cube diagonal <111>, lower along the face diagonal <110>, and lowest along the cube edge <100>. In fact, the Young's modulus in the <111> direction is as much as 2.4 times higher than the modulus in the <100> direction [29]. During the course of the current study, directionality in the mechanical properties was observed. The anisotropy is explained by consideration of the effects of the microstructure present, as well as the effects of the preferred orientation which exists in the material.

The microstructure of the 62# and 78# double-reduced tinplate steels consisted of a fully recrystallized matrix of ferrite. The grains are elongated in the rolling direction, with the so-called pancake grain structure. Materials which have undergone heavy cold

reductions often exhibit mechanical fibering, where second phases and inclusions are elongated and aligned in the rolling direction. The fibering is typically associated with anisotropic mechanical properties, because the inclusion stringers hinder plastic flow of the material varying amounts in different directions in the plane of the sheet.

The microstructure of the sheet steels did not reveal appreciable mechanical fibering, in fact, the material was relatively free of large sized inclusions. When the sheet steel is finish rolled above A_3 and the coiling temperature is kept low, the resulting microstructure consists of recrystallized ferrite grains with small, evenly distributed precipitates. The rapid heating and cooling rates associated with the continuous annealing process produce a relatively fine grain size, and promote the retention of carbon and nitrogen in ferrite solid solution. The resulting microstructure of the final product is relatively "clean," with small, evenly spaced precipitates. The grain-shape effect, however, does play a role in the observed anisotropic properties. As the stress axis varies from 0 to 90° with respect to the rolling direction, grains elongated in the rolling direction become increasingly constrained by contiguous grains. Due to the elongation of the grains, more barriers to slip exist in the form of grain boundaries, and plastic deformation becomes increasingly difficult, resulting in increased strength.

When comparing the strengths of the 62# and 78# plate materials, the smaller grain sized 78# material exhibited higher strength and reduced plastic elongation to failure. The smaller grain size relates to larger grain boundary area. The grain boundaries act as obstacles to dislocation motion, and a larger number of obstacles to plastic flow in the material results in increased strength. For polycrystals, a condition of compatibility between neighboring grains exists during deformation. This accomodation is realized by multiple slip in the vicinity of the boundaries. The smaller the grain size, the larger will be the total boundary surface area per unit volume. Therefore, for a given deformation the total volume occupied by work-hardened material increases with decreasing grain size, resulting in greater hardening due to dislocation interactions induced by multiple slip.

While the microstructural features play a small role in the directionality of mechanical properties, the major cause of anisotropy in rolled steel sheet is attributed to the preferred orientation present in the material. When a material is subjected to large rolling reductions, the individual grains in the polycrystal rotate on their appropriate slip systems under the constraints of the deforming forces. Eventually, a limited number of stable orientations are reached where further reductions do not cause additional reorientation. The stable orientations reached are dependent on many factors, including the crystal structure and processing parameters, and are such that slip occurs easily.

Upon annealing, the texture is altered in a way which is related to the rolling texture. In the case of sheet steel, the {111}<uvw> fiber texture is present through hot-rolling and cold-rolling, and is further enhanced by the annealing process. The texture present in the material allows slip to occur easily when the testing axis is aligned with the rolling direction due to the activation of primary slip systems. Since the orientation difference from grain to grain is minimized due to the preferred orientation, dislocation motion from grain to grain occurs easily. As the testing axis is varied towards 90° with respect to the rolling direction, the applied stress to initiate plastic deformation is increased since secondary slip systems must be activated. Due to the increasing misorientation between neighboring grains, dislocations must change their direction of motion at the grain boundaries, which results in increased strength, reduced ductility and an increase in the strain hardening of the material.

During the standard tensile testing, Lüders band formation was observed during the latter stages of the deformation, with failure occuring at the location of one of these bands. Lüders bands are caused by inhomogeneous yielding, with yielding occuring within but not outside of the bands. Specimens oriented along the rolling direction exhibited a high degree of Lüders band formation, with the bands eventually propagating to cover the entire reduced gage section. As the off-axis angle increased, the amount of observable Lüders band formation decreased, reinforcing the theory of the activation of secondary

slip systems for specimens with increasing off-axis orientation. The main texture component present in the sheet steel specimens was the {111}<uvw> fiber texture, with a continuous orientation spread from {111}<110> to {111}<211>. While the two end points of the above orientation spread are orthogonal to one another with a continuous spread, one might conclude that the properties in the plane of the sheet would be relatively isotropic. However, the texture is much sharper in the rolling direction due to the constraints of the rolling process, leading to anisotropy in the plane of the sheet.

It should be noted that the processing conditions imposed on the double-reduced tinplate steels are such that the directionality of mechanical properties is minimized. The processing parameters associated with the hot-rolling, cold-rolling and continuous annealing operations produce a product which is fully recrystallized ferrite, and is ductile despite its relative hardness. The preferred orientation present imparts directionality in properties due to the inherent anisotropy in the single crystal. However, as a measure of uniformity, the strength of the material varied less than 15% from 0 to 90° with respect to the rolling direction in the plane of the sheet. Thus, this material represents a high quality product which has been engineered to avoid many undesirable properties.

CONCLUSIONS

1. The microstructure of the double-reduced tinplate steel consisted of a fully recrystallized matrix of ferrite grains, with relatively few inclusions and precipitates. While the grain size and average grain volume was larger for the 62# plate material, the aspect ratios of 62# and 78# plate materials were very similar. The smaller grain size of the 78# plate material lead to increased strength and decreased ductility due to the larger total boundary area which impedes dislocation motion.

2. Mechanical testing showed a trend of increased strength and decreased ductility as the testing axis with respect to rolling direction varied from 0 to 90°. The trend in material strength is explained by considering the effects of the grain shape as well as the contribution of the texture associated with the material. The shape of the grains leads to an increase in the number of grain boundary interactions, and increasing misorientation between neighboring grains due to the texture lead to additional impedance to dislocation motion.

3. The popLA software package proved to be a very useful tool in the analysis of the experimentally determined pole figure data. Theoretical texture analysis is extremely complex, requiring mathematically sophisticated techniques. The complexity of the mathematics involved has made it operationally inaccessible to the materials user. The popLA software package performs all of the necessary mathematical computations, many of which could only be performed by mainframe computers a short time ago, and is quite user friendly. The program generates all necessary descriptive texture plots, with very good graphics.

4. Texture analysis results showed the preferred orientation of the sheet steels to consist mainly of a {111}<uvw> complete fiber texture. A partial fiber texture with <110> directions parallel to the rolling direction encompassing orientations of {001}<110>, {112}<110> and {111}<110> was also present to a much smaller degree.

5. While the textures present in the 62# and 78# plate materials were very similar, the skeleton line along the {111}<uvw> γ-fiber revealed a slightly stronger intensity associated with the $\{111\}\langle\bar{1}10\rangle$ orientation for the 62# plate material. The higher intensity can be attributed to the additional grain growth which this material experiences during the continuous annealing cycle, which leads to the growth of $\{111\}\langle\bar{1}10\rangle$ oriented grains at the expense of grains of different orientations.

LIST OF REFERENCES

REFERENCES

1. D.J. Blickwede, Trans. of ASM, **61** (1968) 149-175.

2. W.T. Lankford, N.L. Samways, R.F. Craven, and H.E.McGannon, TheMaking, Shaping, and Treating of Steel, U.S. Steel, Pittsburgh (1985), 1.

3. ibid, 746.

4. ibid, 745.

5. ibid, 788.

6. R.D. Hindson, International Symposium on The Annealing of Low Carbon Steel, The William Feather Company, Cleveland, **1**, (1958) 9-17.

7. R.L. Rickett and F.C. Kristufek, Trans. ASM, **41** (1949) 1113-1141.

8. G. Kudjumov and G. Sachs, Z. Phys., **64** (1930) 225.

9. R.K. Ray and J.J. Jonas, "Transformation Textures in Steels," International Materials Reviews, **35**, No. 1 (1990) 1-36.

10. B.L. Bramfit and A.R. Marder, "Processing and Properties of Low Carbon Steels," Am. Inst. of Mining, Met. and Petroleum Eng., **191** (1973).

11. Vanderschueren, Van Houtte, Aernoudt, Dilewijns and Standaert, Hot Rolling Textures of Low Carbon Steel Sheets and Their Influence on the Texture After Continuous Annealing.

12. The Making, Shaping, and Treating of Steel, 1103.

13. S.S. Gorelik, Recrystallization in Metals and Alloys, MIR Publishing, Moscow, 1981.

14. H. Takechi, H. Kato and S. Nagashima, Trans. AIME, **242** (1968) 56-65.

15. A.J. Heckler and W.G. Granzow, Metall. Trans., **1** (1970) 2089-2094.

16. S. Mishra and C. Därmann, "Role and Control of Texture in Deep-Drawing Steels," International Metals Reviews, 27 (1982) No. 6, 307-320.

17. W.C. Leslie, J.D. Michalak and F.W. Aul, The Annealing of Cold Worked Iron, Iron and its Dilute Solid Solutions, John Wiley & Sons, New York (1963) 119.

18. H. Hu, Trans. AIME, **224** (1962) 75.

19. C.G. Dunn, Acta Met., **2** (1954) 173.

20. J.E. Burke, Trans. AIME, (1952) 263.

21. I.L. Dillamore, C.J.E. Smith and T.W. Watson, Met. Sci. J., 1 (1967) 49-54.

22. J.S. Kallend, U.F. Kocks, A.D. Rollett and H.R. Wenk, Mat. Sci. and Eng., **A132** (1991) 1-11.

23. M. Hatherly and W.B. Hutchison, An Introduction to Textures in Metals, Institution of Metallurgists, London, 1979.

24. R.D. Williams, J. Appl. Phys., **39** (1968) 4329.

25. J. Imhof, Textures and Microstructures, **4** (1982) 189, 5 73.

26. S. Matthies and G. Vinel, Phys. Stat. Sol. (b), **112** (1982) k111-k115.

27. S. Matthies, Proc. 7th ICOTOM, C.M. Brakman, P. Jongenburger, E.J. Mittemeijer eds., Netherlands Society for Materials Science, **1** (1984) 737-751.

28. H.R. Wenk and U.F. Kocks, Met. Trans. A, **18A** (June 1987) 1083-1092.

29. U. Lotter and W. Bleck, Proc. 7th ICOTOM, C.M. Brakman, P. Jongenburger, E.J. Mittemeijer eds., Netherlands Society for Materials Science, **1** (1984) 637-641.